The University of Adelaide

Master of Philosophy (Physical Sciences)
Thesis

Project:
Machine learning for quantitative fibre optic sensing

Darcy Smith
Faculty of Sciences
School of Physical Sciences

Supervisors:
David J. Ottaway
Stephen C. Warren-Smith and Linh V. Nguyen

May 23, 2022

Contents

Abstract

Optical fibre sensing correlates measurable properties of the light guided within an optical fibre with an external parameter being sensed. There are a number of different methods of fibre sensing, including scattering based sensing, specklegram sensing and interferometric sensing, each with their own applications and limitations. Sensing with multimode fibre offers some significant advantages over single mode fibre, but carries the inherent limitation of extracting useful information from the highly complex and sensitive process of multimode fibre transmission.

Deep learning is a form of machine learning at the forefront of data analysis and processing which has solved many problems in a wide range of applications, most notably image and speech recognition. Its application in multimode fibre imaging and sensing has been brief but successful. In this thesis, deep learning is explored as a tool for understanding and quantifying the complex multimode fibre transmission process for sensing applications.

Chapter 2 looks at deep learning applied to fibre specklegram sensing, demonstrating its ability to correlate the change in the specklegram output of the fibre with a parameter of the fibre's environment for temperature and refractive index sensing. The superiority of the deep learning approach over current statistical methods is demonstrated, as the deep neural networks improve upon the issues of limited dynamic range and vulnerability to specklegram misalignment that are present with the correlation method. At the same time, the first example of deep learning for regression-based sensing of a continuous variable, as opposed to discrete/classification sensing, is presented.

Chapter 3 looks at deep learning applied to sensing with the wavelength spectrum output of a multimode fibre. Current methods of interferometric sensing with a wavelength spectrum and multimode fibre involve the need to inscribe resonance-producing structures within the fibre, which can be costly and time-consuming. The use of deep learning has been previously explored

as a method of extracting information pertaining to an environmental parameter, specifically temperature, from a wavelength spectrum without the presence of any resonant features. This thesis looks to build upon such work by demonstrating multi-point sensing using the concept of encoding spatially resolved temperature information in a wavelength spectrum. Sapphire crystal optical fibre is used for sensing, where its highly variable fibre radius is exploited as a means of encoding such spatially resolved information in a fashion that a deep neural network can learn. It is shown that such networks trained on spectra from sapphire fibre perform far better for multi-point temperature sensing than those trained on spectra from glass silica fibres of constant radius.

List of publications

0.1 Published journal articles

Smith, D.L., L.V. Nguyen, D.J. Ottaway, T.D. Cabral, E. Fujiwara, C.M.B. Cordeiro, S.C. Warren-Smith. Machine learning for sensing with a multimode exposed core fiber specklegram sensor. *Opt. Express*, 2021.

0.2 Conference proceedings

Smith, D.L., L.V. Nguyen, D.J. Ottaway, T.D. Cabral, E. Fujiwara, C.M.B. Cordeiro, S.C. Warren-Smith. Machine learning for sensing with a multimode exposed core fibre specklegram sensor. Poster presentation. Australian and New Zealand Conference for Optics and Photonics (ANZCOP), Australia, 18-19 November, 2021.

Smith, D.L., L.V. Nguyen, D.J. Ottaway, S.C. Warren-Smith. Deep learning for distributed fibre temperature sensing. Oral presentation. Australian Institute of Physics (AIP) Summer Meeting, 7-9 December, 2021.

Declaration

I certify that this work contains no material which has been accepted for the award of any other degree or diploma in my name, in any university or other tertiary institution and, to the best of my knowledge and belief, contains no material previously published or written by another person, except where due reference has been made in the text. In addition, I certify that no part of this work will, in the future, be used in a submission in my name, for any other degree or diploma in any university or other tertiary institution without the prior approval of the University of Adelaide and where applicable, any partner institution responsible for the joint award of this degree.

The author acknowledges that copyright of published works contained within the thesis resides with the copyright holder(s) of those works.

I give permission for the digital version of my thesis to be made available on the web, via the University's digital research repository, the Library Search and also through web search engines, unless permission has been granted by the University to restrict access for a period of time.

I acknowledge the support I have received for my research through the provision of an Australian Government Research Training Program Scholarship.

SIGNED

DARCY SMITH

DATE: 29/12/21

List of Acronyms

ANN: artificial neural network

CNN: convolutional neural network

CW: constant wave

DNN: deep neural network

ECF: exposed core fibre

FBG: fibre Bragg grating

FPI: Fabry-Perot interferometer

FSR: free spectral range

FSS: fibre specklegram sensor

GRIN: graded-index fibre

MLP: multi-layer perceptron

MMF: multimode fibre

MSE: mean-squared error

OFDR: optical frequency-domain reflectometry

OPL: optical path length

OTDR: optical time-domain reflectometry

RMSE: root-mean-squared error

SCF: suspended core fibre

SMF: single mode fibre

SOF: sapphire optical fibre

TM: transmission matrix

WDM: wavelength-domain multiplexing

ZNCC: zero normalised cross-correlation

1 Introduction

1.1 Sensing with optical fibres

1.1.1 Overview

The potential of fibre optics technology has been realised since the mid 1960s, with their low loss light transmission properties, revolutionising the telecommunication industry [1]. Interest in fibre optics for sensing applications can be traced to 1967, with the patenting of the "Fotonic Sensor" for surface finish monitoring [2]. Both research interest and industry applications in fibre optics for telecommunications and sensing since these origins have been heavily dominated by the former, due to the immediate market impact and collective research focus, something fibre sensing did not have. Nevertheless, fibre sensing has been extensively researched, with notable commercial successes such as gyroscopes and structural health monitoring [3].

The attractiveness of optical fibres for sensing (as well as telecommunication) purposes stems from the many unique properties of standard glass silica optical fibre; electromagnetic passivity, small size (radius on the order of tens of microns), ability to access difficult to reach locations (such as in vivo), corrosion resistance, and compatibility with technology and systems developed for telecommunication [4, 3]. They are also capable of multiplexing information in the wavelength domain and yielding spatially resolved information in the time domain.

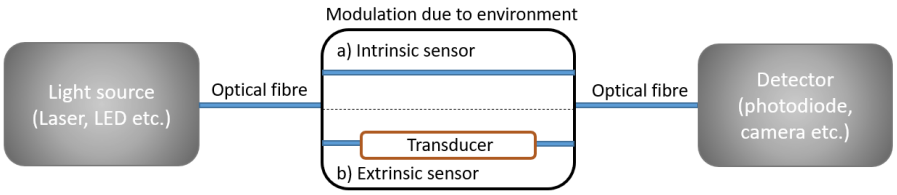

Figure 1: Basic principle of operation of a) an intrinsic and b) an extrinsic optical fibre sensor

Optical fibre sensors operate on the principle that the properties of light

guided within an optical fibre, such as intensity, wavelength, polarisation or phase, can be modulated by the environment surrounding the fibre [4]. This implies that environmental parameters such as temperature, pressure and strain can be correlated with the output of an optical fibre and hence sensed. As shown in Figure 1, if the modulation of the light occurs within the fibre, the sensor is classed as intrinsic, whereas if an external transducer used, wherein the light modulation occurs, the sensor is classed as extrinsic [5].

1.1.2 Theory of light propagation of through optical fibre

Classical geometric ray tracing is the simplest and most intuitive picture to describe the propagation of electromagnetic radiation, and is an approximation which holds when the fibre core size is large compared to the wavelength of light. For almost all conventional fibres, including the fibres used throughout the experimental sections of this thesis, this approximation holds, meaning one can draw results from applying geometric optics to the propagation of light through optical fibres. To do this we consider a circular, step-index fibre, as shown in Fig. 2. A ray of light travelling through the core of the fibre that makes an angle θ_z with the fibre axis will strike the core-cladding interface of the fibre at an angle θ. As per Snell's law of refraction (Eq. 1), there is a critical angle, θ_c associated with this interface (Eq. 2), such that any angle of incidence at or above this angle will result in all of the incident light to be reflected and none to be transmitted through the interface.

$$n_i sin(\theta_i) = n_t sin(\theta_t) \tag{1}$$

$$\theta_c = sin^{-1}(\frac{n_t}{n_i}) \tag{2}$$

Here, n_i and n_t denote the refractive index experienced by the incident and transmitted rays respectively, and θ_i and θ_t denotes the angles these rays

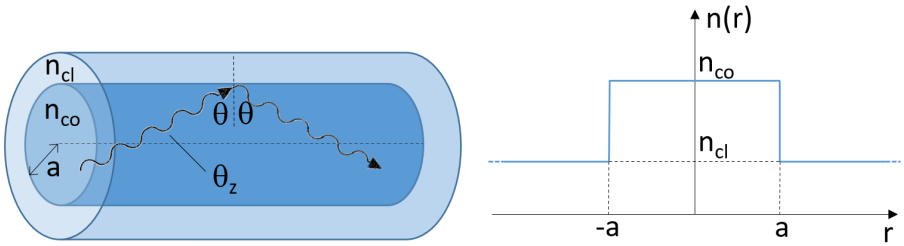

Figure 2: a) A ray of light incident on the core-cladding interface of a step-index optical fibre b) the refractive index profile of a step-index fibre

make with the normal to the interface between the media. Specifically, in the case of a ray of light striking the core-cladding interface of a fibre, $n_i = n_{co}$ and $n_r = n_{cl}$. For a ray of light propagating in a fibre, which makes an angle θ_z with the fibre axis, and angle $\theta = 90^o - \theta_z$ with the normal to the core-cladding interface, propagation without loss of power due to reflections at the core-cladding interface will occur so long as $\theta \geq \theta_c$, or according to the condition in Eq. 3.

$$\theta \geq sin^{-1}(\frac{n_{cl}}{n_{co}}) \tag{3}$$

To fully understand how light exists and propagates through an optical fibre, however, one must use the electromagnetic field picture of light. Maxwell's equations describe the spatial and temporal relationships of the electric and magnetic components of a time varying electromagnetic field, and are given in Eqs. 3-6 [6] as:

$$\nabla \mathbf{H} = \mathbf{J} + \frac{\partial \mathbf{D}}{\partial t} \tag{4}$$

$$\nabla \mathbf{E} = -\frac{\partial \mathbf{B}}{\partial t} \tag{5}$$

$$\nabla \cdot \mathbf{D} = \rho \tag{6}$$

$$\nabla \cdot \mathbf{B} = 0 \tag{7}$$

H denotes magnetic field strength, **J** denotes current density, **D** denotes the electric displacement field, **E** denotes the electric field strength, **B** denotes the magnetic flux density and ρ denotes the electric charge density.

The goal is now to solve for **E** and **H** with the constraints imposed by a fibre's geometry. In this case a translationally invariant, step-index, circular fibre is considered. While the fibres used in the experimental sections of this thesis deviate from translational invariance and a step-index nature, the conclusions drawn from this simple case are enough to gain a general understanding of how light propagates through a fibre. The principles and feasibility of optical fibre sensing can also be drawn from these conclusions. This derivation follows [6].

The step-index, circular fibre has a circularly symmetric cross-sectional refractive index profile, $n(r)$, which can be described in cylindrical polar coordinates (r, φ, z) as:

$$n(r) = \begin{cases} n_{co}, & 0 \leq r < a \\ n_{cl}, & a < r < \infty \end{cases} \tag{8}$$

It can be shown that for a translationally invariant fibre, the z-dependence of the electric and magnetic fields can be separated from the transverse (r and ϕ) dependence in the form of a complex exponential:

$$\mathbf{E}(r, \phi, z) = \mathbf{e}(r, \phi) exp(i\beta z) \tag{9}$$

$$\mathbf{H}(r, \phi, z) = \mathbf{h}(r, \phi) exp(i\beta z) \tag{10}$$

where β denotes the propagation constant of the fibre. It can be shown that satisfying Maxwell's equations in this situation reduces to solving the

vector wave equation in both the core and the cladding, with the condition of continuity of the tangential field components across the interface of the two. In the case of the translationally invariant fibre, this reduces to

$$\{\nabla_t^2 + n^2k^2 - \beta^2\}e_z = 0\,. \tag{11}$$

Here ∇_t denotes the spatial derivative transverse to the fibre axis (z-axis), k the wavenumber and e_z the z-component of the modal field. It can also be shown that, from Maxwell's equations, the transverse modal fields can be determined from e_z once it has been determined from the scalar wave equation.

There is a set of solutions to the scalar wave equation given the boundary conditions, which are indexed by two values: ν and m. These solutions, which we refer to as the supported or guided modes of the fibre, have complex forms. To describe these solutions in simple form, we first define three quantities: U, W and R as follows:

$$U = a(k^2n_{co}^2 - \beta^2)^{1/2} \tag{12}$$

$$W = a(\beta^2 - k^2n_{cl}^2)^{1/2} \tag{13}$$

$$R = r/a \tag{14}$$

Radially, the modes take the form $J_\nu(UR)$ in the core, where J_ν is the ν^{th} Bessel function of the first kind, and $K_\nu(WR)$ in the cladding, where K_ν is the ν^{th} modified Bessel function of the second kind. Azimuthally, the modes take the form $sin(\nu\phi)$ or $cos(\nu\phi)$ depending on their parity. ν is the first of two indices with which modes are identified. Multiple solutions with the same ν index may satisfy the scalar wave equation, however these modes will have different values of β and hence different values of U. Such modes are distinguished by the second modal index m, with the solution possessing the highest value of U given $m = 1$ and so forth.

Azimuthally invariant modes, that is with $\nu = 0$, correspond to the transverse electric and magnetic modes, TE_{0m} and TM_{0m}. Modes with $\nu \geq 1$ are referred to as the hybrid modes, $HE_{\nu m}$.

A quantity used to describe how multimode a fibre is, is its V-number, defined as:

$$V = ak(n_{co}^2 - n_{cl}^2)^{1/2} \tag{15}$$

A fibre with a V-number in the range $0 < V < 2.405$ will operate as a single-mode fibre. The number of supported modes increases as the V number increases. For large V-numbers, the number of supported modes can be approximated with:

$$N_{modes} \approx \frac{V^2}{2} \tag{16}$$

Modes with lower ν become supported before those with higher ν. Standard multimode telecommunications fibres with a core diameter of 50 νm and a numerical aperture (defined as $NA = \sqrt{n_{co}^2 - n_{cl}^2}$) of 0.39 will have a $V \approx 40$, meaning they will support roughly 800 modes.

Intensity interference patterns

The electric field in a fibre is the superposition of the electric fields belonging to each individual supported mode. For a fibre with N supported modes, each with modal coefficient a_j and propagation constant β_j, the electric field cross-section at position z along the z-axis is given by

$$\mathbf{E}(r, \phi, z) = \sum_{j=1}^{N} a_j \hat{\mathbf{e}}_\mathbf{j}(r, \phi) exp(i\beta_j z) \, , \tag{17}$$

where $\hat{\mathbf{e}}_j(r,\phi)$ is the unit vector pointing in the direction of $\mathbf{e}_j(r,\phi)$. The intensity speckle pattern, I, is given by the magnitude of this electric field vector squared,

$$I(r,\phi,z) = \left| \sum_{j=1}^{N} a_j \hat{\mathbf{e}}_\mathbf{j}(r,\phi) exp(i\beta_j z) \right|^2 \tag{18}$$

This intensity speckle pattern, when imaged and recorded, is called a specklegram, and is used for sensing in chapter 2. It is highly sensitive to the phase relations between each pair of modes in the fibre, as seen in the scale of the complex phase term, for which a full 2π phase shift occurs over one effective wavelength of its associated mode.. The dependence of a fibre's refractive index on environmental parameters (such as temperature and pressure), and in turn β_j's dependence on the fibre's refractive index, makes a specklegram highly sensitive to changes in the fibre's environment, a desirable quality of fibre sensors.

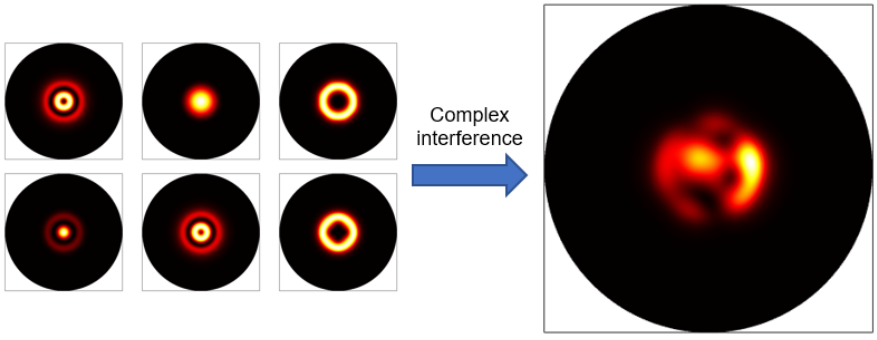

Figure 3: Example of the electromagnetic intensity pattern of individual modes propagating in a fibre (left) and the total intensity pattern, resulting from complex interference between these modes (right).

Fig. 3 shows a numerically modelled example of the cross-sectional intensity pattern belonging to six different supported modes in a fibre, as well as the overall intensity pattern belonging to the superposition of all modes in the fibre. Although the individual modal intensities carry a certain radial

symmetry, the resultant intensity becomes a complex interference pattern due to the phase differences between the modes.

The other piece of data collected from an optical fibre sensor for sensing in this thesis is a wavelength power spectrum, used in chapter 3. This is generated by measuring the power coupled into a single mode fibre from the optical fibre sensor at a range of wavelengths. The act of coupling the light into a single mode fibre filters out the power which does not reside near the fibre's core. As the intensity pattern is dependent upon the wavelength, this power will vary across the wavelength range. In addition, a given wavelength power spectrum will change in response to the fibre's environment through perturbations to the fibre's refractive index and length, and hence can be used for sensing.

The wavelength power spectrum is a superposition of the interference between each pair of modes in the fibre. A pair of modes with differing effective propagation constants will produce a periodic wavelength interference pattern, who's periodicity in wavelength space depends on the difference between these propagation constants. By considering the equation for the full interference pattern given in Eq.18, it can be seen that the contribution for each pair of interfering modes will be given by the cross terms that arise from squaring the summation. The wavelength dependence of this intensity arises from the β_j term, itself given by Eq. 19.

$$\beta_j = \frac{2\pi}{\lambda} n_{eff,j}(\lambda) \tag{19}$$

1.1.3 Selected optical fibre sensors

There are a number of methods of effectively correlating changes in the light guided within an optical fibre to an environmental parameter. Successful methods include interferometric sensing (i.e. Fabry-Perot interferometers (FPIs) and fibre Bragg gratings (FBGs)), scattering based sensing and specklegram sensing. Scattering based sensors have the

ability to be classed as truly distributed, in that sensing information is provided on a continuous spatial scale. Quasi-distributed sensing, that is, distributed sensing at discrete, spatially resolved points, can be achieved via interferometric methods using wavelength division multiplexing. The number of sensing points is limited by the available wavelength bandwidth.

Interferometric sensing

Interferometric sensors aim to create features in the wavelength or frequency spectrum of a beam of light that are easily measured/tracked and correlated to properties of the medium through which the light passed [4]. Early forms of interferometric sensing included Mach-Zehnder [7] and Sagnac [8] interferometers, which split a single mode of light in two beams in order to create an interference pattern with itself as a result of differing optical path lengths. These are capable of sensing anything which affects the optical path length of the light propagating through the fibre, such as temperature and pressure. Alternative versions of interferometric sensors include FPIs and FBGs.

A fibre FPI functions by inscribing a cavity inside of an optical fibre, with reflections from either end of the cavity producing an interference pattern formed from the two reflections [9]. The resulting interference pattern is periodic in wavelength, with the repeating nature corresponding to multiples of 2π in the phase difference between the two reflected beams. The distance between two spectral peaks is called the free spectral range, and is dependent on the refractive index of the medium comprising the cavity. Extrinsic FPIs consist of a cavity of a different material than the fibre, usually air, and produce an interference pattern between reflections from either end of the cavity. Intrinsic FPIs use the fibre itself as the cavity material, usually with mirrors inserted at either end of the desired cavity. FPI interference patterns are characterised by the coefficient of finesse, $\mathcal{F}$ (Eq. 20), a function of the reflectivity of the mirrors comprising the cavity (R_1 and R_2), and determines

how narrow the resonant peaks that are produced are. This is shown in Figure 4.

$$\mathcal{F} = \frac{2\pi}{-ln(R_1 R_2)} \tag{20}$$

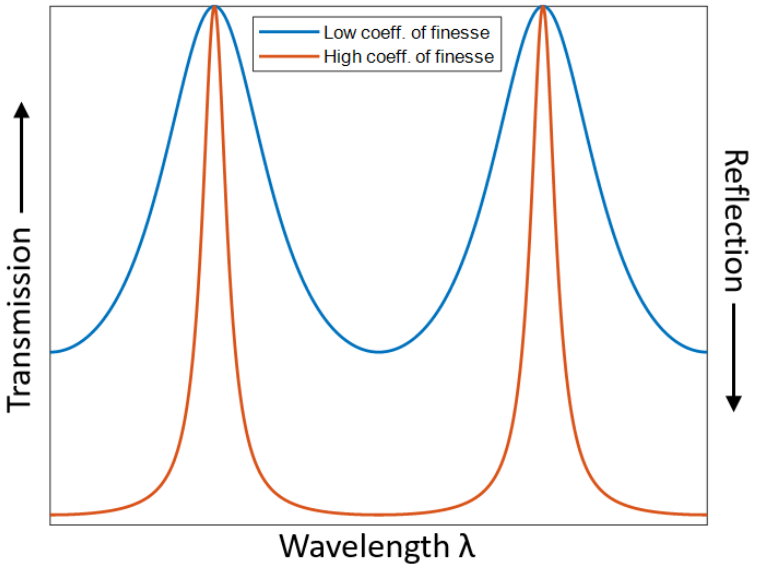

Figure 4: Two interference patterns produced from theoretical Fabry-Perot interferometers with different coefficients of finesse.

FBGs operate on a similar principle to FPIs, in that they aim to produce resonant features in the wavelength spectrum of a fibre that can be easily tracked. An FBG creates a single resonant peak that moves in wavelength space in response to the fibre's optical path length. This is achieved with a periodic perturbation to the fibre's refractive index, called a grating, which scatters light off each perturbation. The rigid spacing of the grating (named the "pitch" and denoted by Λ) creates a resonance condition relating to the spacing between perturbations, given by Eq. 21 [10]. Figure 5 shows this principle of operation.

$$\lambda = 2n_{eff}\Lambda \tag{21}$$

The light reflected from each of the grating perturbations will grow out of phase if this condition is not met, leaving a strong peak in the reflection spectrum at this wavelength. This resonant wavelength is directly related to the refractive index of the fibre and hence will shift in a manner that can be calibrated to sense any environmental parameter which affects the fibre's optical path length.

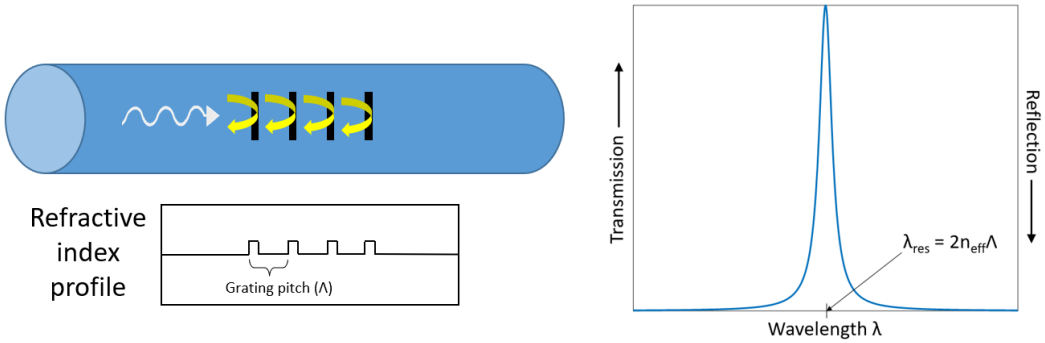

Figure 5: Principle of operation of an FBG. The resonant wavelength is determined by the spacing of the grating and the effective refractive index of the propagating mode in the fibre.

Both Fabry-Perot interferometers and fibre Bragg gratings are capable of operating as multi-point sensors. FBGs can achieve this via two methods; wavelength-division multiplexing, which inscribes multiple gratings of different resonant wavelength in the fibre [11], and time-division multiplexing, which inscribes multiple, low reflectivity gratings in the fibre, who's reflected signals can be distinguished in the time domain [12]. The former is limited in dynamic range by the size of the available wavelength bandwidth, whereas the latter is limited by the available time domain resolution. FPIs can also achieve multi-point sensing through wavelength-division multiplexing in the Fourier domain, but this is more difficult [13]. A novel approach is to inscribe FPIs whose cavities are defined by low reflectivity FBGs. The different cavities can be distinguished using Fourier analysis [14]. In all

cases, inscribing just a single FBG or FPI in an optical fibre can be difficult, costly and time consuming, which poses an inherent difficulty in these sensing methods which increases with the number of sensing points desired.

Scattering based sensing

Truly distributed sensors require continuous sensing at every single point along a fibre to be capable of sensing temperature, not just discrete points, something that is inherently not possible with the interferometric sensing techniques described thus far. This type of sensing can be achieved by exploiting the scattering that occurs everywhere as light propagates in a fibre through mechanisms such as Raman, Rayleigh and Brillouin scattering, as shown in Figure 6. Signals produced by the three types of scattering are sensitive to different environmental parameters, and as such are suitable for different types of sensors. Raman scattering is a result of the interaction between light and thermally excited molecules [15], hence being sensitive to temperature and mainly used for distributed temperature sensing [16]. Brillouin scattering is a result of the interaction between light and an acoustic wave in the given medium acting as a form of Bragg grating, reflecting a wavelength corresponding to its spatial wavelength. The reflected light is dependent on both the medium's refractive index and the wave's acoustic velocity, which are both a function of temperature and strain, allowing Brillouin scattering based sensors to perform distributed temperature and strain sensing [17]. Rayleigh scattering is a result of light interacting with random inhomogeneities in the medium. It is frequently used for distributed acoustic sensing, in conjunction with phase-sensitive optical time domain reflectometry (Φ-OTDR) [18, 19].

Brillouin optical time domain analysis (BOTDA) is the main method of interrogating a distributed sensor based on stimulated Brillouin scattering [20]. This involves sending a pump pulse along the fibre that has a weak CW probe also sent through it. The reflection from the pulse gives information on

the Brillouin scattering due to the probe signal at each point it encounters. Issues with BOTDA include phase noise arising from the coherence of the pump pulse [21], the requirement of polarisation parallelism between pump and probe [22] and trade-off between spatial resolution and pulse width.

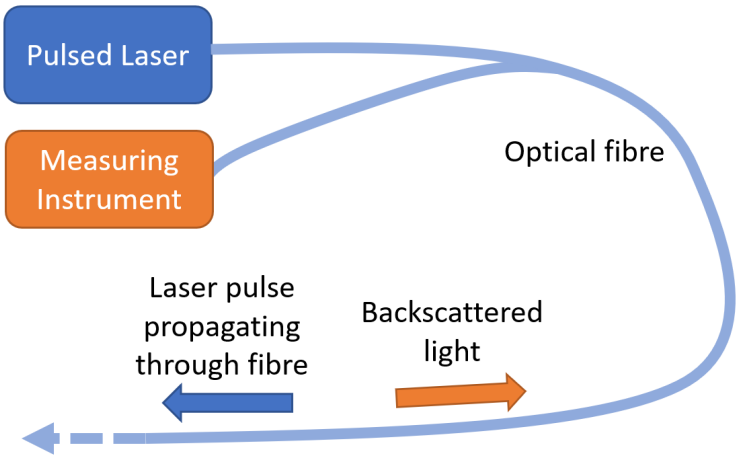

Figure 6: Principle of operation of an OTDR based distributed sensor.

Optical time domain reflectometry (OTDR) is the main method of interrogating a Raman distributed sensor [23]. This operates on the principle that the local Raman backscatter in an optical fibre increases with increasing temperature [16]. The limitation of both of these scattering-based temperature sensing methods is however the spatial resolution being limited by the time domain resolution of the recording equipment.

Specklegram sensing

An optical fibre specklegram sensor (FSS) exploits the sensitivity of the OPLs and relative phases of a fibre's guided modes for sensing. Instead of analysing interference features in the wavelength domain, specklegram sensing utilises the cross-sectional spatial intensity interference pattern emanating from an MMF's end facet [24]. Section 1.1.2 gave an example and the theory behind specklegrams.

FSSs have the advantage of only requiring cheap and lightweight equipment in comparison to other optical fibre interrogation techniques; a lens, webcam and coherent light source is sufficient to capture a specklegram [25]. Given these advantages, they have found many unique applications including motion sensing and surveillance [26, 27, 28], temperature sensing [29, 30] and strain measurement [31]. Some other specific applications include wavelength detection [32] and blood flow monitoring [33].

The methods used to analyse and compare specklegrams are statistical, the two main methods being correlation [34] and subtraction [35]. Such statistical methods suffer from a lack of distributed sensing capabilities, dynamic range limitations and vulnerability to noise, meaning the majority of success in FSS finds itself in qualitative measurements and classification. This thesis will address such weaknesses in specklegram sensing by exploring the use of deep learning for specklegram analysis, demonstrating its superiority over a traditional statistical correlative method in temperature and refractive index (water depth) sensing.

1.2 Deep learning of multimode fibre transmission

1.2.1 Deep learning introduction

Machine learning is a term which encompasses all methods and algorithms by which a computer recurrently 'learns' from a set of data to continually improve its parameters to optimise for a certain task [36]. Deep learning is a branch of machine learning techniques, which uses large sets of data to train neural networks, the architectures of which can loosely be made analogous to the neurons in the human brain (hence the name) [37]. These networks have the potential to be very large in size, with almost every parameter able to be trained via backpropagation and stochastic gradient descent [38]. Deep learning allows such neural networks to learn the representations required for understanding data in high dimensional spaces without any prior human input or knowledge about the data and its domain. Deep neural networks are generally structured with layers which represent the data in increasing levels of abstraction, starting from the raw input and ending with the output.

Deep learning is recognised as the biggest advancement in machine learning over the past 10 years and has become famous as a powerful tool for finding intricate trends and structures in potentially very highly dimensional data. Its potential came to the fore at the 2012 ImageNet competition for classifying images, in which convolutional neural networks far outperformed all other algorithms [39]. Some of its most well-known and successful applications aside from image recognition include language processing [40], speech recognition [41] and autonomous vehicle navigation [42]. Deep neural networks gain the ability to learn a more comprehensive set of the representations required to characterise its given dataset the larger and more diverse the dataset is. The applications mentioned above all have readily available corresponding datasets which are large and diverse, which contributes to their status as deep learning's largest successes. In reality though, deep learning has shown itself to be capable of learning high-

dimensional structures in any dataset, hence its wide variety of uses and applications.

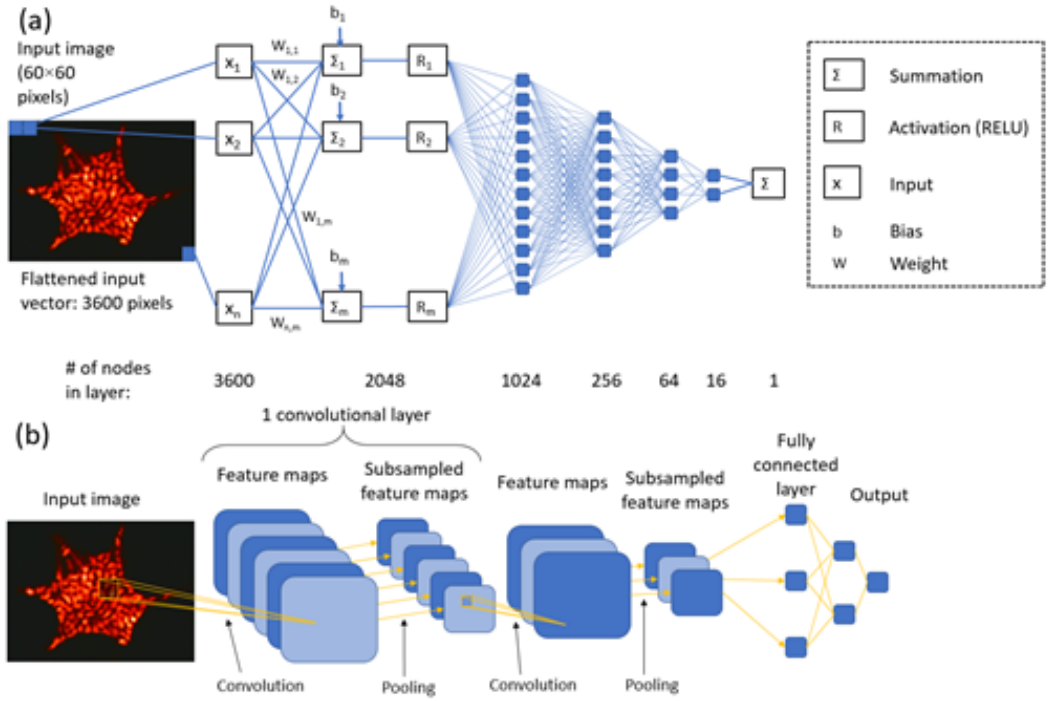

Figure 7: Schematic representations of a) a multi-layer perceptron and b) convolutional neural network

Two classes of deep neural network are used in this thesis; multi-layer perceptrons (MLP) [43] and convolutional neural networks (CNN) [44]. Schematics of these are displayed in Fig. 7. MLPs are one of the simplest DNN architectures and consist of a series of layers of nodes, the input layer being the raw data and the output layer being the desired output of the network. Each node's value is determined as a linear combination of the nodes in the previous layer, with a nonlinear activation function. The weights (coefficients) and biases (constants) comprising these linear combinations are the trainable parameters of the model. MLPs take a one-dimensional input, so higher dimensional data must be flattened to a vector before training an MLP.

CNNs use convolutional windows, called filters, to scan the input data,

performing correlations between the filter's values and the data's. These filter values are the trainable parameters of the CNN. The model attempts to maximise the correlation value, hence optimising the filters as representations of adjacent datapoints in the data. This makes CNNs capable of not only learning recurrent features in images and other data, but recognising these features no matter where they appear. This is an advantage over MLPs, which can learn features but only when they appear in the same location in the data (hence activating the same nodes). A consequence of this is that CNNs are far more computationally expensive than similarly sized MLPs.

1.2.2 Deep learning for multimode fibre transmission and imaging

The transmission of light through a multimode fibre is a complex and highly sensitive process meaning it can be difficult to quantify and control. However, it can be advantageous to use MMF over single mode fibre where the complexity of the MMF transmission can be exploited, particularly for sensing where the output is highly sensitive to perturbations. For these reasons and applications, it is relevant to attempt to understand MMF transmission process. A theoretical framework which solves for the allowed modes in a fibre and their propagation characteristics in the ideal case has been well established [6, 45]. However, this theory is unable to account for the imperfect nature of fibres, which sustain deviations from their ideal forms during the fabrication process. The effects of these imperfections grow with the length of the fibre and can render the transmission process highly unpredictable, yet still deterministic.

Methods of determining and controlling the MMF transmission process empirically have been used as a means of accounting for this unpredictable nature. The transmission matrix of a fibre is an experimentally determined map between its input and output, and digital holography is a means of shaping the input to a fibre in order to reverse engineer its output [46, 47, 48]. Plöschner et. al. (2015) used a spatial light modulator and knowledge of the transmission matrix of a MMF to fully quantify the transformation of light

from input to output, as well as demonstrating the ability to shape a fibre's output to an arbitrary amplitude distribution [49], even showing robustness against deformities and bends in the fibre. However, these methods are highly vulnerable to perturbations on the fibre which introduce temporal changes in the specklegram for a constant input, especially for longer fibres.

The use of an artificial neural network for MMF imaging dates back to 1990, with Aisawa et al. (1990) using an ANN for image classification from 10 categories of images transmitted through a MMF [50]. This method employed a three-layer MLP with sigmoid activation, and investigated image classification amongst image displacement and the introduction of artificial noise. More recently, it has been shown that convolutional neural networks (CNNs) are a powerful tool in MMF imaging. Borhani et. al. (2018) demonstrated the reconstruction and classification of an image set of handwritten digits through a MMF of length up to 1 km using a "visual geometry group" (VGG) CNN [51]. Rahmani et al. (2018) trained both a VGG and a "Resnet" CNN for amplitude-amplitude inversion and amplitude-phase inversion for image reconstruction again on handwritten digits. Transfer learning, specifically the networks successfully reconstructing specklegrams into handwritten symbols not seen during training, was also demonstrated [52]. These authors have more recently demonstrated MMF image reconstruction in the presence of wavelength drift [53]. Caramazza et al. demonstrated the reconstruction of natural scene images transmitted through a MMF from the specklegram [54]. Other instances of the use of deep learning in conjunction with specklegrams include the interrogation of FBGs [55] and wavelength detection [56].

1.2.3 Deep learning for sensing with multimode fibre

The current literature on deep learning for MMF sensing is less numerous than that of deep learning for MMF imaging. The limited examples include deep learning applied to scattering based sensing [57, 58, 59], specklegram sensing [60, 61] and wavelength spectrum sensing. The majority of these

demonstrate classification based sensing [62], with only two examples of regression based sensing.

Deep learning has been applied to the OTDR-interrogated scattering signal from a MMF for a number of purposes. Various CNNs have been shown to be able to classify a variety of different classes of mechanical perturbations and the location they occurred from an OTDR scattering signal [57, 58]. The input data to the networks in this case consisted of three-dimensional matrices; the three axes representing time, distance along the fibre and the backscattered signal strength. In [58], these matrices spanned 120 s and 33 km and were fed into a CNN. Another example of deep learning applied to scattering-based sensors is the detection of structural micro-cracks in the fibre used for sensing [59]. Despite these qualitative, classification based applications of deep learning in scattering sensing, little to no research exists of deep learning in a regression sensing context, such as temperature and pressure sensing.

There are limited examples of deep learning applied to other forms of sensing. Cuevas et al. (2018) used MMF specklegram output to classify the location of mechanical perturbations on the fibre [60], similar to [57] and [59]. In this example, the subtraction between a resting specklegram and one recorded while the fibre was being mechanically perturbed was fed into both a CNN and MLP with the goal of predicting the discrete section of fibre that the perturbation took place. This is the only example so far of deep learning for spatially resolved sensing without using scattering based methods. The fibre used for the experiment was bent in a continual 'S' shape, and although it is not addressed in the paper, this thesis will address the fact that induced mode mixing can give an optical fibre distributed sensing capabilities.

There are limited examples of deep learning for regression sensing with MMF. Nguyen et al. [62], the lead author of which co-supervised the research comprising this thesis, demonstrated deep learning for temperature sensing using the wavelength transmission spectrum of a sapphire crystal

optical fibre. The spectra were collected while the fibre was simultaneously subjected to strong mechanical noise, demonstrating a deep neural network's ability to extract information pertaining to a measurand of choice from a MMF output, even in the presence of strong noise. Smith et al. [61] demonstrated deep learning for regression sensing using the specklegram output of a multimode exposed core fibre, improving upon current statistical methods of specklegram analysis.

1.3 Thesis summary

This thesis demonstrates the potential of deep learning for MMF sensing. It will build upon the current literature by training DNNs for sensing in two experiments. Chapter 2 demonstrates for the first time regression specklegram sensing using deep learning, which, similar to [60], trains a DNN on the specklegram output of a MMF, but trains it to sense a continuous range of a parameter of interest as opposed to simply classifying a discrete location. Chapter 3 builds upon [62] by training a DNN for temperature sensing using the wavelength spectrum from a MMF, this time demonstrating multi-point, spatially resolved sensing by giving the DNN multiple, spatially resolved temperature labels along the fibre's length to learn.

Both of these examples of deep learning applied to MMF sensing are at the forefront given they are using a DNN designed for regression sensing, something which has only been used once before in the literature. The majority of sensing applications of deep learning perform classification, which is often a simpler concept to prove. However, for quantitative sensing requirements, such as temperature and pressure sensing, it is regression sensing that is required. This thesis aims to provide a base for deep learning applied to both specklegram and wavelength spectrum sensing, successfully demonstrating the first example of regression-based sensing with either of these MMF outputs.

2 Deep learning for fibre specklegram sensing

2.1 Introduction

Current methods of analysing and comparing specklegrams for various applications use purely statistical methods, for example correlation [34] and differencing [35] in the context of fibre specklegram sensing as well as decorrelation techniques in the form of principal component analysis for data filtering [63] and speckle noise reduction [64]. A downside of these methods is that they can lose information in the specklegram images; for example correlation sums the contributions of all pixels into a single value to quantify the similarities between two specklegrams. As a result, much of specklegram sensing is aimed towards qualitative and classification applications, such as motion detection and mechanical perturbation event classification.

Cabral et al. (2020) demonstrated the use of a multimode exposed core fibre (ECF) for fibre specklegram sensing [29]. This publication demonstrated fibre specklegram sensing of temperature and refractive index on a continuous scale using a statistical correlation method. Despite functioning as a proof of concept, the limitations of the correlative method become known in the form of a dynamic range limitation. This method quantifies how different a specklegram is from a reference specklegram based on the zero-normalised cross correlation (ZNCC) function, and identifies this with how far the chosen measurand has shifted from its reference point. Once the specklegram images reach zero correlation with the reference, further changes will not give any useful information and the dynamic range has been reached.

The research publication presented in this chapter applies deep learning techniques to the same dataset as [29] to demonstrate not only the ability for a DNN trained on fibre specklegram data to perform regression sensing, but to improve upon the limitations imposed on the current correlation methods.

2.2 Publication

Statement of Authorship

Title of Paper	Machine learning for sensing with a multimode exposed core fiber specklegram sensor
Publication Status	☐ Published ☒ Accepted for Publication ☐ Submitted for Publication ☐ Unpublished and Unsubmitted w ork w ritten in manuscript style
Publication Details	Accepted for publication in Optics Express

Principal Author

Name of Principal Author (Candidate)	Darcy Smith		
Contribution to the Paper	Darcy was the primary researcher for this publication. He contributed to the conceptualisation of the work, performed the machine learning analysis, and drafted the manuscript.		
Overall percentage (%)	70%		
Certification:	This paper reports on original research I conducted during the period of my Higher Degree by Research candidature and is not subject to any obligations or contractual agreements with a third party that would constrain its inclusion in this thesis. I am the primary author of this paper.		
Signature		Date	30 December 2021

Co-Author Contributions

By signing the Statement of Authorship, each author certifies that:

i. the candidate's stated contribution to the publication is accurate (as detailed above);

ii. permission is granted for the candidate in include the publication in the thesis; and

iii. the sum of all co-author contributions is equal to 100% less the candidate's stated contribution.

Name of Co-Author	Linh Nguyen		
Contribution to the Paper	Linh contributed to the conceptualisation of the research, the machine learning model framwork, the interrpretation of the results, and edited the manuscript.		
Signature		Date	4 February 2022

Name of Co-Author	David Ottaway		
Contribution to the Paper	David contributed to the conceptualisation of the research, the interpretation of results and edited the manuscript.		
Signature		Date	4 February 2022

Please cut and paste additional co-author panels here as required.

Name of Co-Author	Cristiano Cordeiro		
Contribution to the Paper	Cristiano fabricated the optical fibre, contributed to the analysis of the speckle data and edited the manuscript.		
Signature		Date	December 11, 2021

Name of Co-Author	Thiago Cabral		
Contribution to the Paper	Thiago collected the original data used for the machine learning analysis (published elsewhere) and edited the manuscript.		
Signature		Date	27 December 2021

Name of Co-Author	Eric Fujiwara		
Contribution to the Paper	Eric contributed to the analysis of the speckle data and edited the manuscript.		
Signature		Date	24 December 2021

Name of Co-Author	Stephen Warren-Smith		
Contribution to the Paper	Stephen contributed to the conceptualisation of the research, fabrication of the optical fibre, interpretation of the results and editing the manuscript.		
Signature		Date	14 December 2021

Research Article | Vol. 30, No. 7 / 28 Mar 2022 / Optics Express 10443

Optics EXPRESS

Machine learning for sensing with a multimode exposed core fiber specklegram sensor

DARCY L. SMITH,[1,*] LINH V. NGUYEN,[1] DAVID J. OTTAWAY,[1] THIAGO D. CABRAL,[2,3] ERIC FUJIWARA,[3] CRISTIANO M. B. CORDEIRO,[1,2] AND STEPHEN C. WARREN-SMITH[1,4,5]

[1] *Institute for Photonics and Advanced Sensing and School of Physical Sciences, The University of Adelaide, Adelaide, SA 5005, Australia*
[2] *"Gleb Wataghin" Institute of Physics, University of Campinas, Campinas 13083-859, Brazil*
[3] *School of Mechanical Engineering, University of Campinas, Campinas 13083-860, Brazil*
[4] *Australian Research Council Centre of Excellence for Nanoscale BioPhotonics, The University of Adelaide, SA 5005, Australia*
[5] *Future Industries Institute, University of South Australia, Mawson Lakes, SA 5095, Australia*
[*] *darcy.smith@adelaide.edu.au*

Abstract: Fiber specklegram sensors (FSSs) traditionally use statistical methods to analyze specklegrams obtained from fibers for sensing purposes, but can suffer from limitations such as vulnerability to noise and lack of dynamic range. In this paper we demonstrate that deep learning improves the analysis of specklegrams for sensing, which we show here for both air temperature and water immersion length measurements. Two deep neural networks (DNNs); a convolutional neural network and a multi-layer perceptron network, are used and compared to a traditional correlation technique on data obtained from a multimode fiber exposed-core fiber. The ability for the DNNs to be trained against a random noise source such as specklegram translations is also demonstrated.

1. Introduction

Optical fibers as sensors have been extensively researched, and notable commercial applications include gyroscopes and structural health monitoring [1]. Interest in this technology is due to the properties of optical fiber sensors (OFSs), including their light weight, small size, absence of moving parts, and resistance to electromagnetic fields [1–4]. Generally, an OFS functions by correlating changes in an external measurand of choice (such as temperature, strain or pressure) [5], with measurable changes in the phase, polarization or intensity of the light propagating through it. A particularly sensitive approach is to measure the phase properties of the propagating light through interference methods. After propagating through the fiber, the phase of the light at the output depends on the optical path length (OPL), which depends on the effective refractive index of the propagating mode, as well as any perturbations on the fiber affecting its refractive index and length. Directly tracking changes in the phase of light is not feasible due to its very high frequency. Therefore, phase changes are often measured through interferometric techniques such as Fabry-Perot, Mach-Zehnder or, in the case of multimode fiber (MMF), interference between propagation modes.

A specklegram is the total intensity pattern at the end facet of the fiber, and consists of bright and dark features of constructive and destructive interference caused by the relative phases between the modes [6]. Fiber specklegram sensors (FSSs) are OFSs that use an MMF's specklegram to quantify changes in these relative phases. Given the OPL of each mode will respond differently in the presence of environmental changes, the relative phases between these modes and hence the specklegram becomes highly sensitive to the environment surrounding the fiber [7]. FSSs also have the advantage of only needing low cost, lightweight interrogation

#443932 https://doi.org/10.1364/OE.443932
Journal © 2022 Received 27 Sep 2021; revised 27 Nov 2021; accepted 28 Nov 2021; published 15 Mar 2022

Optics EXPRESS

equipment. A lens, coherent light source and webcam is enough to capture a specklegram [8,9] so they have found many unique applications, including motion sensing and surveillance [10,11], strain sensing [12], vibration sensing [7], temperature sensing [13] and wavelength detection [14]. The analysis and comparison of specklegrams from an FSS generally follows one of two statistical methods. The first, correlation, relies on multiplying the pixels of two specklegrams together in order to correlate them and hence uses their similarity as images [7,15]. The second, differencing, relies on subtracting the pixels of the two images in order to use their differences as images [11,16].

Despite the numerous applications FSSs have found solutions for, the current methods of analyzing and comparing specklegram images are at heart purely statistical. The cumulative effect of external perturbations is averaged along the fiber, furthermore, all pixels in the specklegram contribute to a single value quantifying a correlation/difference [8]. In this way, they do not offer any physical insight into how the multimode transmission is occurring throughout the length of the fiber, nor do they offer distributed sensing capabilities, and suffer dynamic range limits. The MMF transmission process is so sensitive to small perturbations that building a mathematical model to describe the transmission can be complex and often limited to special cases. Research has been done in describing the physical transmission of light through an MMF such as building transmission matrices (TMs) [17,18] and phase conjugation [19,20], with applications in imaging and biomedical sensing, for example microscopy [21] and endoscopy [22]. Despite such successes, these analytical methods are highly vulnerable to changes in the fiber's environment, such as bends or defects. Furthermore, they are not suitable for sensing purposes, as the nonlinear effects of environmental changes on MMF transmission go beyond the capabilities of a linear transmission matrix.

The use of deep learning has been explored as a solution to describe MMF transmission by inferring the relationship between an input and a speckle pattern without the need for prior knowledge of the physics and fiber properties governing the transmission [23,24]. A deep neural network (DNN) is a tool to map between potentially very high dimensional data using a non-linear transformation with many parameters, through statistical learning [25]. Deep learning can be considered state of the art in terms of artificial intelligence, displaying capabilities to learn complex patterns in high-dimensional spaces, and solve problems in many fields, most notably image and speech recognition [26,27]. The power of DNNs has also been explored in the context of mapping the complex MMF transmission. Two maps of interest that DNNs are able to learn in regards to MMF transmission include imaging, where the fiber's environment is held constant and a map is learnt between the input and output of the fiber [23,28–32], and sensing, where the input of the fiber is held constant and a map is learnt between the fiber's environment and its output [33,34]. To date, the sensing application of DNNs has been far less explored compared to imaging.

We have previously demonstrated the use of a statistical correlation method [13]; the zero-normalized cross correlation (ZNCC) function, to make an FSS out of a multimode exposed core fiber (ECF). An ECF is a microstructured optical fiber with one side open to the external environment, allowing sensing of external materials through the evanescent field [35]. We have previously demonstrated the use of such a fiber as a suitable tool for biological sensing [36–38]. In this work we utilize two DNN architectures to analyze the change of specklegrams from such an ECF with respect to temperature and refractive index in the form of variable water immersion, the latter of which is only made possilengthble by use of the ECF which allows media of different refractive indices to be in contact with the core of the fiber. We emphasize that the fiber environment is designed to have minimal external perturbations and noise other than the measurand of interest so as to provide a controlled proof of concept. For a demonstration of a DNN's ability to extract a measurand amongst strong noise, see our previous work [33]. We

Optics EXPRESS

demonstrate that two different DNNs improve on the ZNCC method by extending the dynamic range of the sensor, as well as demonstrating robustness against specklegram image translations.

2. Concept and experiment design

2.1. Experimental Principle

The light guided along an optical fiber can be expressed as a superposition of orthogonal modes, each being a unique solution to Maxwell's equations given the boundary conditions imposed by the fiber geometry. At a distance L from the entrance to the fiber, the field transverse to the direction of propagation can be expressed as a superposition of guided modes, as in Eq. (1),

$$\vec{E}(x, y, z = L) = \sum_{i=1}^{N} a_i \hat{e}_i(x, y) e^{i \frac{2\pi}{\lambda} n_{eff,i} L}, \tag{1}$$

where i sums over the N guided modes supported by the fiber, $\hat{e}_i(x, y)$ are the modal fields (unit electric fields), a_i are the modal coefficients (amplitude of each mode), $e^{i \frac{2\pi}{\lambda} n_{eff,i} L}$ is the complex phase term, and $n_{eff,i}$ is the effective refractive index of the i^{th} mode. For the electric field at the end facet of the fiber, L will be the length of the fiber. The specklegram is then the intensity pattern at the end facet of the fiber, which can be expressed as in Eq. (2).

$$I(x, y, L) = \left| \sum_{i=1}^{N} a_i \hat{e}_i(x, y) e^{i \frac{2\pi}{\lambda} n_{eff,i} L} \right|^2 \tag{2}$$

The specklegram's characteristic speckle effect comes from interference between the modes, with bright regions corresponding to constructive interference (modes in phase) and dark regions corresponding to destructive interference (modes with a π phase difference). Figure 1 shows the specklegram from an ECF being imaged using a lens, which can then be captured using a camera or webcam.

The OPL that each mode experiences is given by the product of its effective refractive index and the geometric length travelled ($OPL = n_{eff} L$). All non-degenerate modes will have phase differences along the fiber due to differing n_{eff}. The sensitivity of these phase differences are highlighted by the fact that a full cycle of phase (2π) for modes in a fiber has a length of λ / n_{eff}, which is on the order of microns. The output specklegram is also highly sensitive to deviations from an ideal fiber such as noise or fiber defects. In the ideal case of no noise, a specklegram will change continuously and deterministically with a continuous change in the fiber's environment, but this breaks down in the presence of strong noise. This leads to the idea that specklegrams can be used to sense changes in a fiber's environment, provided noise is not too strong.

Figure 2 shows three specklegrams, each from air temperatures 3°C apart. Although to the human eye it is apparent the specklegram is changing, and the movement/evolution of some features are able to be tracked, the overall trend governing this change cannot be easily determined, and certainly not extended beyond this temperature range. Statistical methods compare how specklegrams differ or correlate pixel to pixel in order to quantify this trend. They can, however, suffer from limited dynamic range as the images become increasingly different from the reference image and further changes in the specklegram reveal less information about how the specklegram has changed. Hence, in this work, we demonstrate that deep learning is a more powerful tool for mapping the seemingly arbitrary relationship between a fiber's specklegram and its environment over a larger dynamic range, improving both accuracy and robustness against unwanted noise. We have previously demonstrated this approach using deep learning on the wavelength dependent transmission spectrum of a multimode fiber coupled to a single mode fiber, rather than specklegram, under strong noise conditions for temperature sensing [33].

Optics EXPRESS

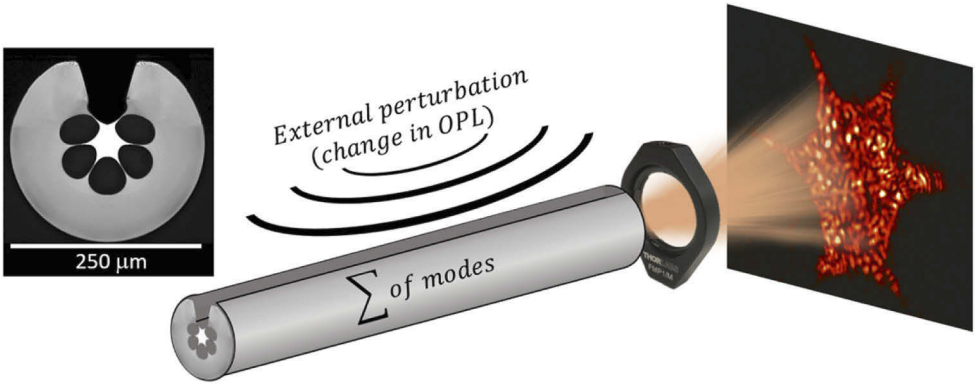

Fig. 1. Representation of multimode transmission of light through an exposed core fiber. The electric field in the fiber is a sum of all its modes. These modes and their relative phases respond differently to external perturbations. A lens is used to image the intensity pattern (specklegram) at the end facet. Also displayed is a cross-sectional image of the fiber used. Reprinted from [13].

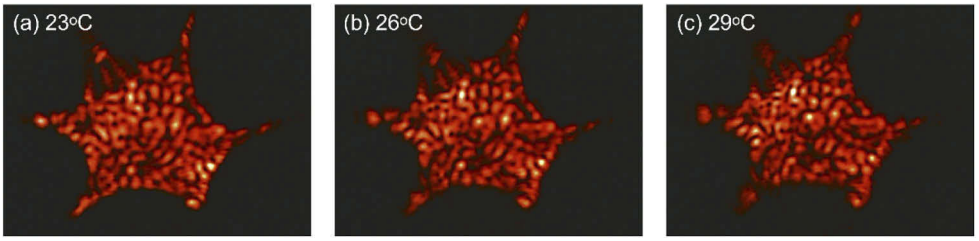

Fig. 2. Specklegrams at the end facet of the ECF corresponding to temperatures of (a) 23°C, (b) 26°C, and (c) 29°C.

2.2. Experimental setup and data collection

The ECF used in this experiment was fabricated by drilling six holes into a pure silica preform using an ultrasonic CNC machine [13]. A diamond endmill was used to open a slot, exposing one of the holes to the outside environment. It was drawn with an optical fiber draw tower at 2005°C. An example cross-sectional image of the fiber is shown in Fig. 1. The length of ECF used for temperature and sensing was 13 cm and 11 cm respectively. This length finds a balance between the sensitivity required to resolve temperature changes, and the dynamic range. water immersion length

The experimental setup, shown in Fig. 3, consisted of a He-Ne laser beam (633 nm, 5 mW) passing through a neutral density filter before being launched into the ECF via a 20× microscope objective lens, and from the end facet of the ECF imaged onto a webcam via a 40× microscope objective lens. The ECF was placed in a fiber bathing apparatus manufactured out of an aluminium block with a Peltier device underneath, to control temperature and water immersion length. The webcam captured footage at an 800×600 resolution and at 15 frames per second. For each discrete temperature/immersion length, approximately 10 seconds of footage was taken, with each frame producing a single specklegram for use in analysis. This resulted in approximately 150 specklegrams per measurand label. The specklegrams within each video differ in that they are affected by inherent noise in the fiber's environment and electrical noise in the webcam. Temperature data was taken in increments of 0.5°C over a range of 22.5-30°C, while immersion length data was taken in increments of 5 mm over a range of 0-50 mm. These ranges were chosen

Optics EXPRESS

as the easiest to achieve while capturing the ZNCC's full dynamic range. For more information about the experimental setup and fiber fabrication, see our previous work [13].

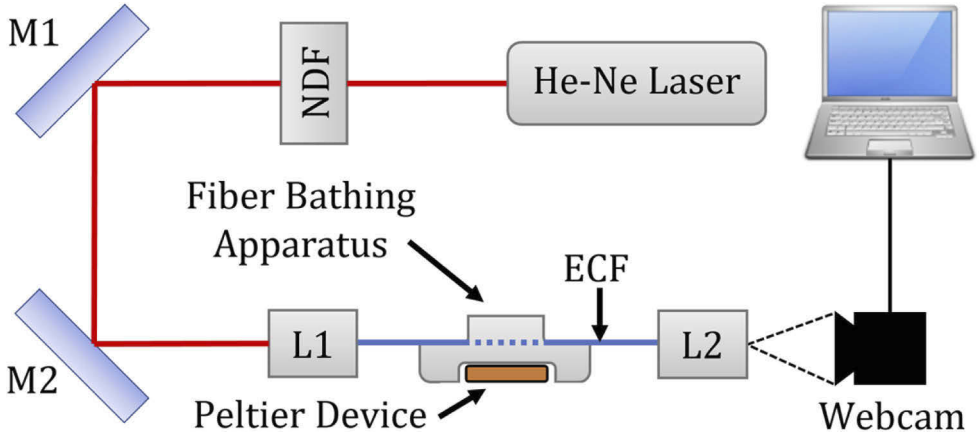

Fig. 3. Schematic diagram of the experimental setup used to capture specklegrams from an ECF in the presence of temperature and refractive index changes. NDF, neutral density filter; M1, M2, mirrors; L1, 20× microscope objective; L2, 40× microscope objective; ECF, exposed core fiber. Reprinted from [13].

2.3. Zero-normalized cross-correlation (ZNCC)

The correlative statistical technique used in our previous work [13], and again included in this paper for comparison is the zero-normalized cross correlation (ZNCC) function, defined in Eq. (3):

$$Z(k) = \frac{\sum_N (I_0 - \bar{I}_0)(I_k - \bar{I}_k)}{\left[\sum_N (I_0 - \bar{I}_0)^2 \sum_N (I_k - \bar{I}_k)^2\right]^{\frac{1}{2}}}, \tag{3}$$

where I_0 is the pixel intensity of a reference frame, I_k is the pixel intensity of the k^{th} frame, the barred intensities are the average pixel intensity for those frames and N sums over all the pixels. The function multiplies two images' corresponding pixels and sums over these pixels to quantify how closely the images are correlated. 1 denotes the images being highly positively correlated, -1 being highly negatively correlated, with 0 being no correlation.

In this work we use a similar image processing method as in [13]. The 800×600 images were cropped to a 200×200 region of interest in order to eliminate the black region surrounding the specklegram. These were then downsampled to 60×60 images in order to save computational power when training the DNNs.

Once the ZNCC scores for each specklegram in a dataset were calculated against the reference frame, a sixth order polynomial calibration curve for the measurand versus ZNCC score curve was fitted. This function was used to make predictions on specklegrams unseen during the calibration process and quantify the performance of the method.

2.4. Deep neural networks (DNNs)

Two broad classes of DNNs, both used in this work, include multi-layer perceptrons (MLPs) [39] and convolutional neural networks (CNNs) [40]. MLPs consist of a series of fully-connected layers, ending with a layer the size of the number of categories to classify or regression variables to calculate. Each node in each layer gets its value from a weighted sum of all nodes in the previous layer. Images and higher dimensional data must be flattened to a single vector before

Optics EXPRESS

passing through an MLP. On the other hand, a CNN uses convolutional layers, each consisting of a set number of convolutional filters that scan the image, calculating a correlation with the corresponding image pixels at each possible position, generating feature maps that hold spatial information as to the image's features. MLPs value each connection between each node equally, whereas CNNs will prioritize connections between adjacent datapoints/pixels, which can be useful for learning recurring features in images.

Firstly, we used an MLP, schematically represented in Fig. 4. When flattened, the 60×60 input image meant our input layer had 3600 nodes. Our output layer, given it was predicting a single value (either temperature or immersion length), had just one node. In between were five hidden dense layers, each decreasing in size from the input size to a single node, a common tactic in MLP architecture design. These hidden layers are there to learn the latent space of the input data in order to facilitate the regression output layers. The rectified linear unit (ReLU) activation [41] was applied after each layer. The model had in total 9,752,929 trainable parameters.

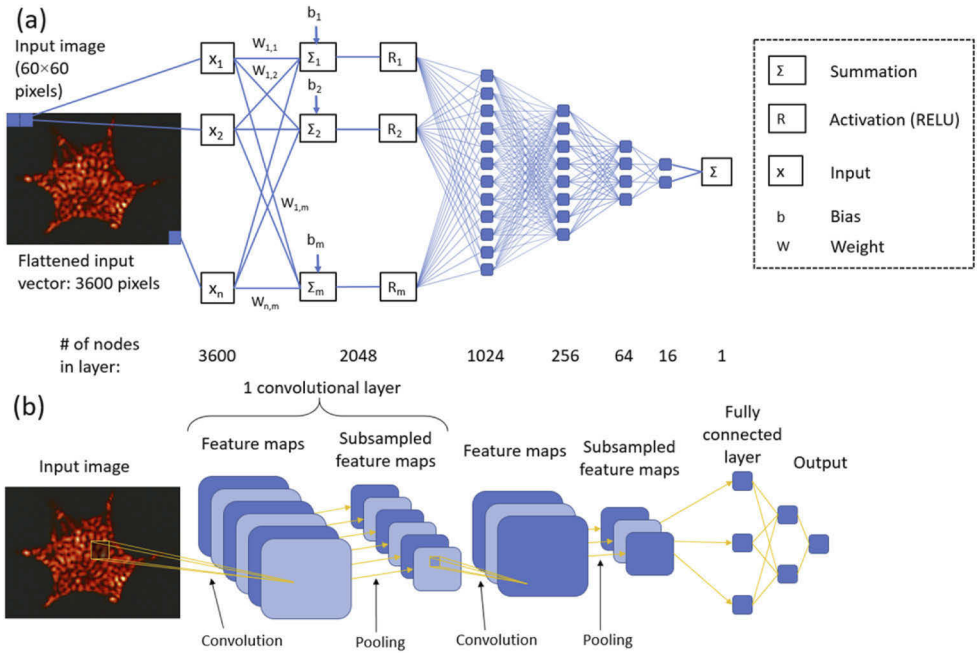

Fig. 4. (a) Schematic of the multi-layer perceptron DNN (MLP) used. The pixel values of the input image are flattened to a single vector and make up the input layer, followed by a series of fully-connected layers. Each node's value is determined by a sum of the contributions from all nodes in the previous layer. The output layer has one node which represents our desired measurand label. (b) Schematic representation of a convolutional neural network (CNN). Each convolutional layer consists of a set number of convolutional filters, each one creating a "feature map", which is a map of correlations as the filter scans the image. These feature maps are then down sampled using a pooling method, comprising one convolutional layer.

Secondly, we used a CNN architecture based on the VGG-16 architecture, a winner at the ImageNet Challenge 2014 image recognition competition [42]. Despite many follow-up architectures being developed since, the VGG architecture continues to work well for many image recognition applications [43,44], as well as for MMF transmission [23]. The architecture features three VGG 'blocks', each consisting of two or three convolutional layers followed by a maxpooling layer [45], which downsamples the result by pooling pixels together and taking

Optics EXPRESS

the maximum value of each 'pool'. Our architecture's three blocks featured two, two and three convolutional layers with 64, 128 and 256 convolutional filters each respectively. Following the third block, the result was flattened and passed through four fully-connected layers, finishing with a single node. All convolutional and dense layers also used the ReLU activation. The model had in total 29,787,329 trainable parameters. This appears as a very large number of parameters, but we believe models of this size are justified given the highly complex nature of the specklegram, which depends on interference between every possible pair of supported modes in the fiber. The ECF used in this research is very highly multimodal, supporting thousands modes, which indicates just how many degrees of freedom such a specklegram depends on. We also believe the use of DNNs over simpler methods of high-dimensional data mapping, such as a supported vector machine [46], is justified. Such methods often require prior knowledge about the domain of the data in order to find and visualize high-dimensional trends, and, while computationally lighter, can be more time consuming overall.

The entire image dataset consisted of approximately 150 specklegrams per measurand label. For the temperature and water immersion length datasets, this was a total dataset of 2,414 and 1,684 specklegrams respectively. These datasets were shuffled and split into three sets; the training set (67.5%), validation set (22.5%), and testing set (10%). The training set was used to train the model while the validation set was used for evaluating the results of this training with images the model had not seen during training. The testing dataset was kept aside during this process and was only seen by the models whilst producing the final results which appear in this paper. This procedure was also used for the ZNCC method, utilizing the same training set for the calibration curve and the same test set for evaluation (the validation set was not used for the ZNCC method as this method has no hyperparameters to tune).

The training process for both models followed a standard procedure. Mini-batches of 64 training samples were randomly sampled from the training dataset and passed through the model. The standard mean squared error (MSE) loss was then calculated. Backpropagation was then performed, whereby the gradient of the loss function with respect to the model's weights was calculated, and these weights adjusted in the negative direction of this gradient, in order to head towards a model with a lower loss value [47]. After this had been completed for all training samples in the training set, one epoch was completed, and the process repeated. Both models were trained for 100 epochs. The Adam optimizer [48] was used with a learning rate of 10^{-3}. After 100 epochs, the model with the lowest MSE loss was taken as the best model and used for making predictions. This length of training was chosen to coincide roughly with the loss value beginning to converge to its apparent minimum. Given the relatively small training dataset size, it was important to not overtrain the model, as this could lead to overfitting and poor generalisation capabilities.

The training was done using a Lenovo Legion 7i laptop with a 10^{th} Gen Intel Core i7-10875H processor, 16 Gb of memory and an NVIDIA GeForce RTX 2070 graphics card. The CNN took generally just under an hour to train 100 epochs with a training dataset of ~1500 specklegrams, while the MLP could do this in minutes.

To quantify the performance of both the DNN models and the ZNCC method, an MSE metric was used in the training. A root mean square error (RMSE) metric is used to display results in this paper in order to preserve the original predictions' units.

3. Results

3.1. ZNCC calibration curve

To make predictions for the measurand associated with a specklegram using the ZNCC method, a sixth order polynomial calibration curve was fitted to the plot of the measurand label against the ZNCC score for each specklegram in the training set against the reference specklegram. This

Optics EXPRESS

curve then returned a predicted measurand when given the ZNCC score of a specklegram in the test set.

From the plots in Fig. 5, it is seen that an ideal curve passing through each of the points would not be a 1-to-1 function, and hence cannot be used for sensing over the full range of temperature and immersion parameters. This is because the calibration curve needs to return a unique measurand label when given a ZNCC score, whereas it is seen in Fig. 5 that the sensor response reaches a minimum ZNCC score of around 0 and then starts increasing again with continually increasing temperature/immersion. This defines a range limit on the ZNCC method, as once the calibration curve is no longer 1-to-1, it can no longer be used for making unique predictions. It is this fundamental limit of the ZNCC method that we will improve upon by employing DNNs

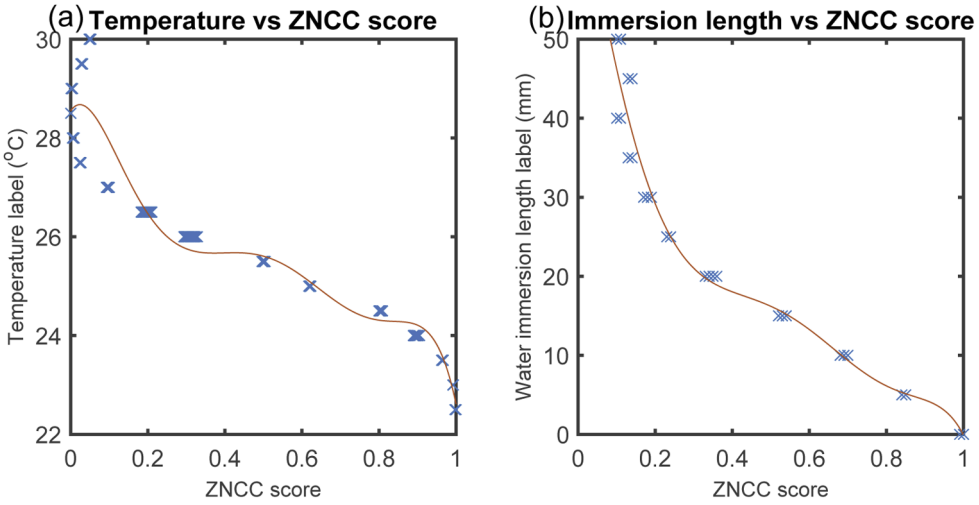

Fig. 5. Calibration curves for predicting (a) air temperature and (b) water immersion length from the ZNCC score of a specklegram against the reference. The fitted curve is a 6^{th} order polynomial.

3.2. Predictions

The results come in three parts. The first two relate to datasets for temperature and water immersion length sensing, while the third looks at the performance of the analysis methods against randomly translated specklegrams. For the first two parts, each of the two datasets (temperature and immersion length) were treated in the same way. The DNNs were trained and a measurand vs ZNCC score function fitted using the training dataset, then the quality of the models tested by making predictions using the testing dataset. For both the temperature and immersion datasets, two methods were performed. The first is as described, where all data was shuffled and split into training/validation/test sets. For the second method, all data relating to three of the labels (23°C, 26°C and 29.5°C for temperature and 5 mm, 25 mm and 45 mm for immersion) were removed from the dataset prior to the split. These labels were chosen so as to have two labels close to either end and one from the middle of the datasets removed. These models were then trained and tested with the given training/testing sets as normal, but then additionally made to make predictions using the data from temperatures/immersions they had not yet seen. This is to simulate how these methods would be expected to function as real world sensors; sensing any measurand value within the trained range despite only seeing a set of discrete labels during training. Results of these tests are shown in Fig. 6 and Fig. 7.

Optics EXPRESS

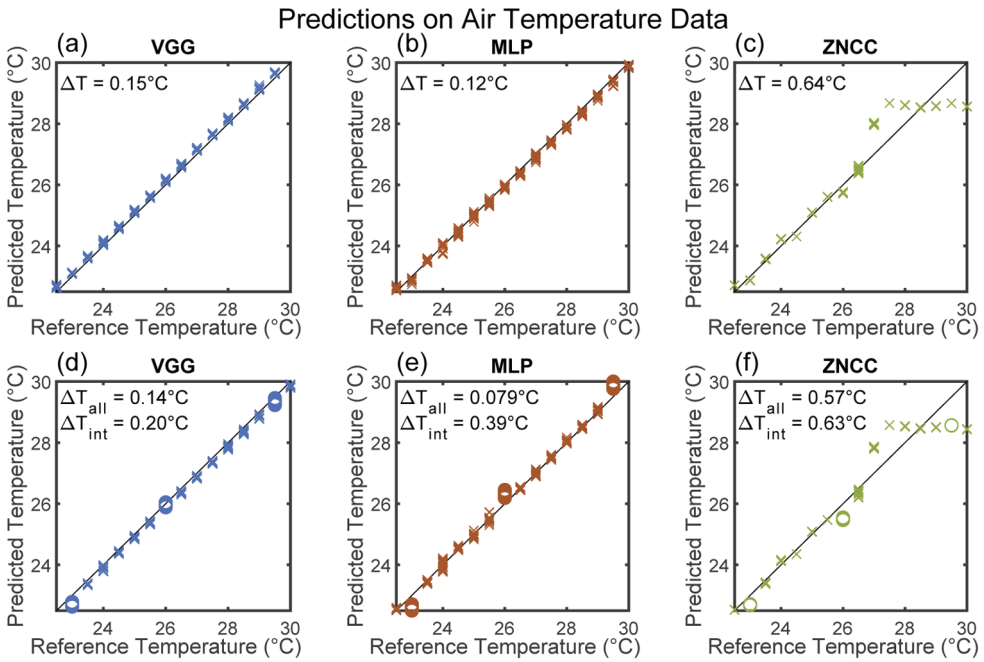

Fig. 6. Ability of the three models to predict temperature labels from specklegrams. (a), (b), (c). All data shuffled and split into training/validation/testing sets, predictions shown made on the test set. (d), (e), (f). Data pertaining to three temperatures removed before the split of data and training. Crosses - predictions on test set, circles - predictions on unseen temperature data. For both: black line - line of parity, i.e. where correct predictions would lie. The ΔT errors shown use a root-mean-square metric. ΔT_{all} refers to the crosses, i.e. temperature labels which the models were trained on. ΔT_{int} refers to the circles, i.e. interpolated predictions on the temperature labels not seen during training.

For the method where all data was combined and shuffled (with no datapoints omitted), the predictions made by the DNNs all lie almost exactly on the line of correct predictions. The ZNCC method's predictions lie close to the line within the useful part of the calibration curve, but become inaccurate as the edge of the correlation range is reached. This demonstrates the inherent range limitation that the ZNCC method possesses, and it can be seen that the DNNs solve this.

For the second part of the analysis, where datapoints were removed so as to interpolate with, the DNNs appear to still make accurate predictions on the data they were trained on, but mostly worse than when they were trained on all data. This can be attributed to the reduced training set size, as the overall distribution of data is smaller and easier to overfit to. The discrepancy is more noticeable in the immersion length set, which we can be attributed to two potential causes. Firstly, the immersion length data contains less labels, and hence removing three points resulted in a greater relative reduction in the datapoints shown in training. Secondly, given the experimental setup, the immersion length reference measurement (data label) has larger relative error compared to temperature, and as such there may be minor inconsistencies in the labelling of the specklegrams that are not present in the temperature dataset

The interpolated points were predicted best by the more complex VGG network, with the MLP showing a more noticeable deviation from the reference labels with these predictions. The ZNCC results for this second part of the analysis are similar to the first part.

Optics EXPRESS

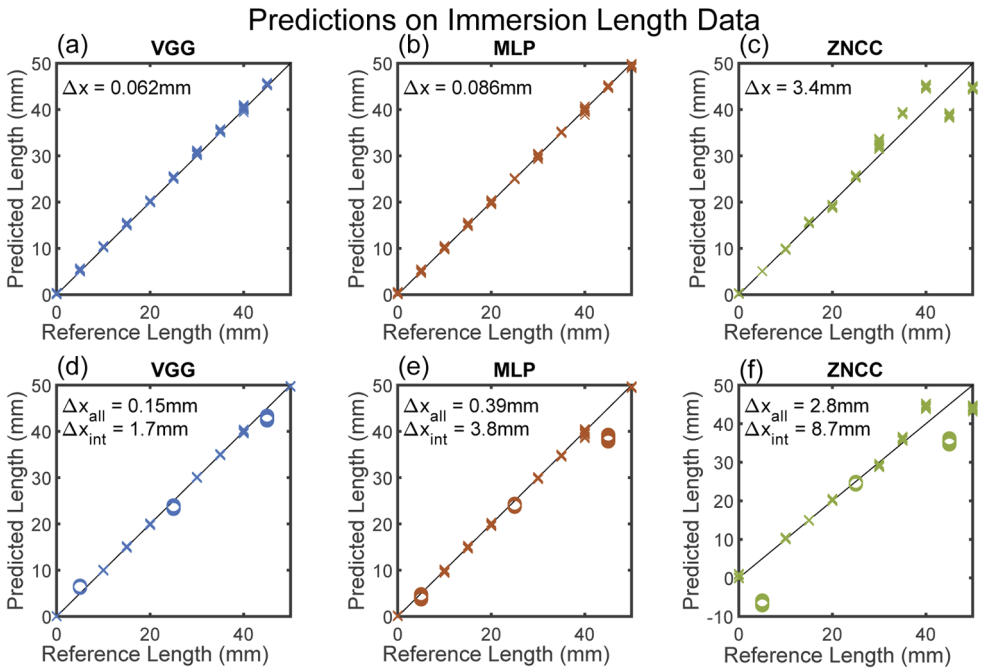

Fig. 7. Ability of the three models to predict water immersion labels from specklegrams. (a), (b), (c). All data shuffled and split into training/validation/testing sets, predictions shown made on test set. (d), (e), (f). Data pertaining to two temperatures removed before the split of data and training. Crosses - predictions on test set, circles - predictions on unseen water immersion data. For all: black line - line of parity, i.e. where correct predictions would lie. The ΔT errors shown use a root-mean-square metric. Δx_{all} refers to the crosses, i.e. water immersion labels which the models were trained on. Δx_{int} refers to the circles, i.e. interpolated predictions on the water immersion labels not seen during training.

3.3. *Translated specklegrams*

After the performance of the DNNs and the ZNCC method had been tested on the two sets of data, the final part of the experiment was to test their robustness against random horizontal and vertical translations of the specklegrams. The capturing of the specklegram via a lens and a webcam requires precise alignment. Therefore this process has the potential to introduce transverse translation due to alignment drift. We have chosen to demonstrate the ability of the CNN to automatically compensate for this type of drift, which is not a feature of the correlation function approach.

To test this, the same procedure as in the first two parts of the experiment was carried out with the temperature data, i.e. all the data was shuffled, split, the models trained/ZNCC curve fitted and predictions were made with varying degrees of random specklegram translations in the vertical and horizontal directions. The physical translation size when the specklegram reaches the webcam, after cropping and downsampling, is equivalent to approximately 0.1 mm per pixel. For each translation amount, the models trained on this data made predictions on the testing set. The results are presented as a plot of model accuracy (average error) against the maximum size of the translations, displayed in Fig. 8.

When the DNNs were shown translated images during the training phase, they were able to effectively learn the measurand/specklegram relation for that size of translation, and achieve an error only a factor of around three away from the original, untranslated specklegram analysis at

Optics EXPRESS

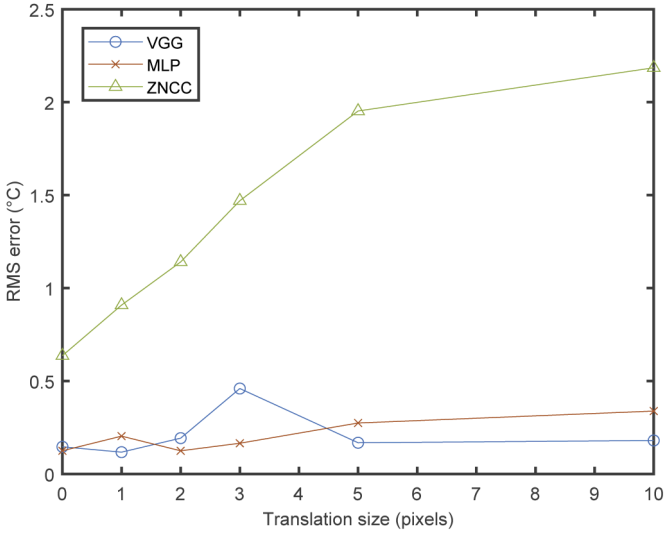

Fig. 8. Performance of the three tested models when trained using artificially translated specklegrams. The x-axis shows the maximum number of pixels that each specklegram in the set could have been translated by in either direction – the actual amount was chosen randomly with a uniform distribution between the positive and negative of the value displayed on the x-axis.

the largest translation size that was tested. The ZNCC method on the other hand begins to diverge in error at even the smallest translation size. It appears to plateau at an RMSE of ~2.2°C, which turns out to be the maximum error possible as it begins predicting a singular average value for all measurand labels. This is to be expected, as the ZNCC method is simply directly comparing images pixel for pixel, so as images for the same label become more different and their ZNCC scores spread over a larger range, it becomes difficult to fit an accurate prediction curve to the data. At the larger translation sizes, spreads of ZNCC scores were so great that a straight line predicting the same temperature for every specklegram minimized the error.

4. Conclusion

We have demonstrated the ability of deep neural networks to learn the complex relationship between changes in a multimode fiber's environment (namely temperature and refractive index), and the intensity specklegram it outputs at its end facet. We have achieved higher accuracy and consistency over a larger measurand range than with a traditional statistical correlation (ZNCC) method. Furthermore, we have demonstrated that deep neural networks (DNNs) are able to learn this multimode fiber transmission relationship even when the training and testing specklegrams have been translated, something the correlation method is fatally vulnerable to. Finally, the feature recognition ability of convolutional neural networks (over both the MLP and ZNCC method) was exploited to predict measurands from translated specklegrams, even when none were included in the training dataset.

This work provides the first direct comparison of a standard statistical method to the use of DNNs in fiber specklegram sensing. We have shown that limitations for the ZNCC method are easily handled by the DNNs, prompting the possibility of further work in the use of DNNs with FSSs and testing what their true limitations are.

This approach of using deep learning for sensing with an exposed core fiber has potential to be useful in biosensing, where the exposed core fiber excels. The use of DNNs could improve

Optics EXPRESS

the versatility of sensors immensely, providing robustness against imaging alignment difficulties and dynamic range issues. Finally, the field of machine learning is vast, and the limits of its application to sensing and imaging are far from being reached. meaning further improvements from the deep learning aspect of this paper are to be expected.

Funding. ARC Future Fellowship (FT200100154); Optofab node of the Australian National Fabrication Facility utilizing Commonwealth and South Australian State Government funding; ARC Centre for Nanoscale BioPhotonics (CE14010003); Fundação de Amparo à Pesquisa do Estado de São Paulo (2018/10409-7).

Disclosures. S.C.W.S. is a director of HT Sensing Pty. Ltd., a company that manufactures optical fiber sensors. HT Sensing Pty. Ltd. did not contribute to or participate in this research in any way.

Data availability. Data underlying the results presented in this paper may be obtained from the authors upon reasonable request.

References

1. B. Lee, "Review of the present status of optical fiber sensors," Optic. Fiber Technol. **9**(2), 57–79 (2003).
2. D. A. M. Krohn, T. W. MacDougall, and A. Mendez, *Fiber Optic Sensors: Fundamentals and Applications*, Fourth Edition ed., (SPIE, 2015), (Chap. 2).
3. X. Wang and O. S. Wolfbeis, "Fiber-Optic Chemical Sensors and Biosensors (2015–2019)," Anal. Chem. **92**(1), 397–430 (2020).
4. K. T. V. Grattan and T. Sun, "Fiber optic sensor technology: An overview," Sens. Actuators, A **82**(1-3), 40–61 (2000).
5. R. A. Potyrailo, S. E. Hobbs, and G. M. Hieftje, "Optical waveguide sensors in analytical chemistry: today's instrumentation, applications and trends for future development," Fresenius' J. Anal. Chem. **362**(4), 349–373 (1998).
6. S. Wu, S. Yin, and F. T. S. Yu, "Sensing with fiber specklegrams," Appl. Opt. **30**(31), 4468–4470 (1991).
7. W. Spillman, B. Kline, L. Maurice, and P. Fuhr, "Statistical-mode sensor for fiber optic vibration sensing uses," Appl. Opt. **28**(15), 3166–3176 (1989).
8. H. S. Efendioglu, "A review of fiber-optic modal modulated sensors: Specklegram and modal power distribution sensing," IEEE Sens. J. **17**(7), 2055–2064 (2017).
9. A. G. F. Leal-Junior, A. C. Marques, and M. J. Pontes, "Optical Fiber Specklegram Sensors for Mechanical Measurements: A Review," IEEE Sens. J. **20**(2), 569–576 (2020).
10. 1M. Englund, A. Ipatti, and P. Karioja, "Fiber optic security monitoring sensor," Proc. SPIE **3099**, 281–296 (1997).
11. A. Dhall, J. K. Chhabra, and N. S. Aulakh, "Intrusion detection system based on speckle pattern analysis," Experimental Techn. **29**(1), 25–31 (2005).
12. S. C. Schneider, Y. Gautam, and B. G. Zagar, "Application of a locally operating laser-speckle strain sensor," IEEE Trans. Instrum. Meas. **52**(4), 1025–1029 (2003).
13. T. D. Cabral, E. Fujiwara, S. C. Warren-Smith, H. Ebendorff-Heidepriem, and C. M. B. Cordeiro, "Multimode exposed core fiber specklegram sensor," Opt. Lett. **45**(12), 3212–3215 (2020).
14. B. Yang, I.-M. Lee, and B. Lee, "Wavelength detection using optical fiber speckle patterns," in *Proc. IEEE 13th Annu. Meeting Lasers Electro-Opt. Soc.*, (2000), pp. 470–471.
15. B. Gupta, H. N. Bhargaw, and H. K. Sardana, "Qualifying fiber optic temperature sensor using speckle metrology," Int. Inf. Technol. Knowl. Manage. **1**, 337–350 (2008).
16. P. Klokoc, I. Lujo, M. Bosiljevac, and N. Burum, "Optical sensor system for vibration measuring," in *Proc. IEEE 50th Int. Symp. ELMAR*, (2008), pp. 625–628.
17. M. Plöschner, T. Tyc, and T. Čižmár, "Seeing through chaos in multimode fibers," Nat. Photonics **9**(8), 529–535 (2015).
18. M. N'Gom, T. B. Norris, E. Michielssen, and R. R. Nadakuditi, "Mode control in a multimode fiber through acquiring its transmission matrix from a reference-less optical system," Opt. Lett. **43**(3), 419–422 (2018).
19. A. Yariv, "Phase conjugate optics and real-time holography," IEEE J. Quantum Electron. **14**(9), 650–660 (1978).
20. I. N. Papadopoulos, S. Farahi, C. Moser, and D. Psaltis, "Focusing and scanning light through a multimode optical fiber using digital phase conjugation," Opt. Express **20**(10), 10583–10590 (2012).
21. B. Silvio and R. Di Leonardo, "A multi-mode fiber probe for holographic micromanipulation and microscopy," Lab. Chip **12**(3), 635–639 (2012).
22. Y. Choi, C. Yoon, M. Kim, T. D. Yang, C. Fang-Yen, R. R. Dasari, K. J. Lee, and W. Choi, "Scanner-free and wide-field endoscopic imaging by using a single multimode optical fiber," Phys. Rev. Lett. **109**(20), 203901 (2012).
23. N. Borhani, E. Kakkava, C. Moser, and D. Psaltis, "Learning to see through multimode fibers," Optica **5**(8), 960–966 (2018).
24. P. Caramazza, O. Moran, R. Murray-Smith, and D. Faccio, "Transmission of natural scene images through a multimode fiber," Nat. Commun. **10**(1), 2029 (2019).
25. Y. LeCun, Y. Bengio, and G. Hinton, "Deep learning," Nature **521**(7553), 436–444 (2015).
26. A. Krizhevsky, I. Sutskever, and G. Hinton, "ImageNet classification with deep convolutional neural networks," Proc. Advances in Neural Information Processing Systems **25**, 1090–1098 (2012).
27. G. Hinton, "Deep neural networks for acoustic modeling in speech recognition," IEEE Signal Process. Mag. **29**(6), 82–97 (2012).

Optics EXPRESS

28. S. Aisawa, K. Noguchi, and T. Matsumoto, "Remote image classification through multimode optical fiber using a neural network," Opt. Lett. **16**(9), 645–647 (1991).
29. R. K. Marusarz and M. R. Sayeh, "Neural network-based multimode fiber-optic information transmission," Appl. Opt. **40**(2), 219–227 (2001).
30. U. Kürüm, P. R. Wiecha, R. French, and O. L. Muskens, "Deep learning enabled real time speckle recognition and hyperspectral imaging using a multimode fiber array," Opt. Express **27**(15), 20965–20979 (2019).
31. W. Xiong, B. Redding, S. Gertler, Y. Bromberg, H. D. Tagare, and H. Cao, "Deep learning of ultrafast pulses with a multimode fiber," APL Photonics **5**(9), 096106 (2020).
32. E. Kakkava, N. Borhani, B. Rahmani, U. Teğin, C. Moser, and D. Psaltis, "Deep Learning-Based Image Classification through a Multimode Fiber in the Presence of Wavelength Drift," Appl. Sci. **10**(11), 3816 (2020).
33. L. V. Nguyen, C. C. Nguyen, G. Carneiro, H. Ebendorff-Heidepriem, and S. C. Warren-Smith, "Sensing in the presence of strong noise by deep learning of dynamic multimode fiber interference," Photonics Res. **9**(4), B109–B118 (2021).
34. A. R. Cuevas, M. Fontana, L. Rodriguez-Cobo, M. Lomer, and J. M. Lopez-Higuera, "Machine Learning for Turning Optical Fiber Specklegram Sensor into a Spatially-Resolved Sensing System. Proof of Concept," J. Lightwave Technol. **36**(17), 3733–3738 (2018).
35. F. M. Cox, R. Lwin, M. C. J. Large, and C. M. B. Cordeiro, "Opening up optical fibers," Opt. Express **15**(19), 11843–11848 (2007).
36. L. V. Nguyen, K. Hill, S. Warren-Smith, and T. Monro, "Interferometric type optical biosensor based on exposed-core microstructured optical fiber," Sens. Actuators, B **221**, 320–327 (2015).
37. S. C. Warren-Smith, H. Ebendorff-Heidepriem, T. C. Foo, R. Moore, C. Davis, and T. M. Monro, "Exposed-core microstructured optical fibers for real-time fluorescence sensing," Opt. Express **17**(21), 18533–18542 (2009).
38. S. C. Warren-Smith, E. Sinchenko, P. Stoddart, and T. M. Monro, "Distributed fluorescence sensing using exposed-core microstructured optical fiber," IEEE Photonics Technol. Lett. **22**(18), 1385–1387 (2010).
39. T. Hastie, R. Tibshirani, and J. Friedman, *The Elements of Statistical Learning: Data Mining, Inference, and Prediction* (Springer, New York, 2009).
40. S. Albawi, T. A. Mohammed, and S. Al-Azawi, "Understanding of a convolutional neural network," in *2017 International Conference on Engineering and Technology (ICET)*, (IEEE, 2017).
41. R. H. R. Hahnloser, R. Sarpeshkar, M. A. Mahowald, R. J. Douglas, and H. S. Seung, "Digital selection and analogue amplification coexist in a cortex-inspired silicon circuit," Nature **405**(6789), 947–951 (2000).
42. K. Simonyan and A. Zisserman, "Very deep convolutional networks for large-scale image recognition," in *ICLR*, (2015).
43. M. Rezaee, Y. Zhang, R. Mishra, F. Tong, and H. Tong, "Using a VGG-16 Network for Individual Tree Species Detection with an Object-Based Approach," in *2018 10th IAPR Workshop on Pattern Recognition in Remote Sensing (PRRS)*, (IEEE, 2018), pp. 1–7.
44. Q. Guan, Y. Wang, B. Ping, D. Li, J. Du, Y. Qin, H. Lu, X. Wan, and J. Xiang, "Deep convolutional neural network VGG-16 model for differential diagnosing of papillary thyroid carcinomas in cytological images: a pilot study," J. Cancer **10**(20), 4876–4882 (2019).
45. D. Scherer, A. Muller, and S. Behnke, "Evaluation of pooling operations in convolutional architectures for object recognition," in *Intl. Conf. on Artificial Neural Networks*, (2010), pp. 92–101.
46. B. E. Boser, I. M. Guyon, and V. N. Vapnik, "A training algorithm for optimal classifiers," in *Proceedings of the 5th Annual ACM Workshop on Computational Learning Theory*, 144–152.
47. D. E. Rumelhart, G. E. Hinton, and R. J. Williams, "Learning representations by back-propagating errors," Nature **323**(6088), 533–536 (1986).
48. P. K. Diederik and J. Ba, "Adam: A Method for Stochastic Optimization," in *3rd International Conference for Learning Representations*, (2015).

2.3 Additional information to the publication

2.3.1 Loss, overfitting and underfitting

Two problems commonly occurring within the realm of deep learning which are important to monitor for and avoid are underfitting and overfitting. Overfitting occurs when a model learns the training data too well, that is, memorises the noise and peculiarities of the training dataset as if they were characteristic of the entire data distribution. As a result, overfitted models find it difficult to generalise to the validation set, which was drawn from the same distribution of data as the training set. Overfitting is characterised by the loss value on the validation set diverging upwards as the training loss converges to its minimum, and is commonly an issue when using small datasets. Underfitting occurs when a model is unable to learn the basic trends within a dataset, and is characterised by the training loss failing to converge to a sufficiently low value, and is usually an indicator of no strong correlation between the x- and y-data or a model not complex enough to find a correlation [65].

As the dataset used for the training in this experiment could be considered small for deep learning, there was a potential for the models being trained to overfit. With this consideration in mind, two steps were taken. Firstly, the number of training epochs was kept to 100, so that the model may have enough time to fit to the training data without overfitting and losing its ability to generalise to the validation and test sets. Secondly, the validation loss history was monitored alongside the training loss, in case it diverged upwards while the training loss converged. Figure 8 shows the training and validation loss histories for the models trained on all data (that is, without omitted labels for testing interpolation). As shown in this figure, the validation loss converges with the training loss rather than diverging, indicating no overfitting present with these models.

As the loss history plots seemingly converge close to their minimum value by as early as 20 epochs, the argument could be made that even 100 epochs

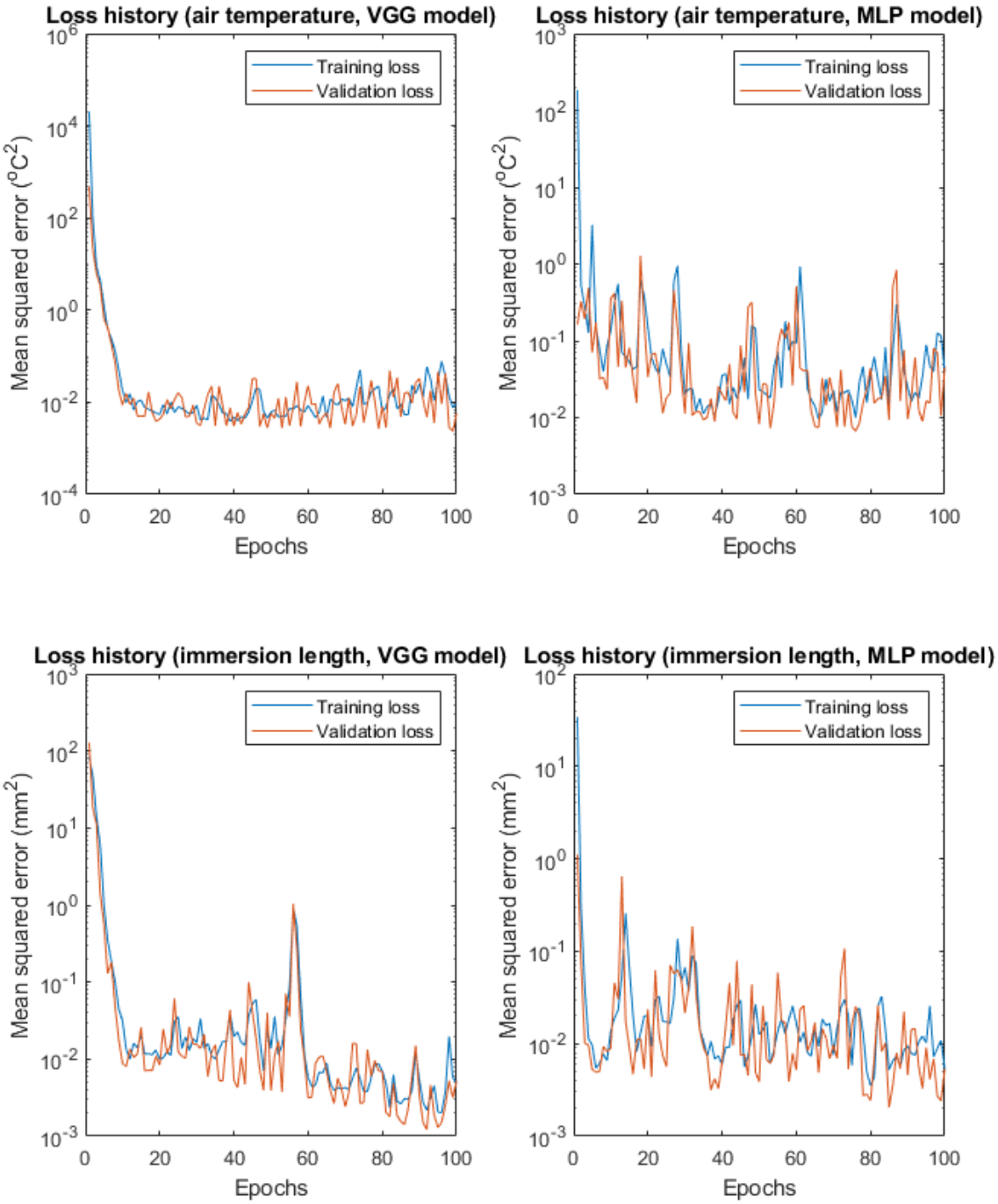

Figure 8: Training and validation loss history of four models trained during the experiment.

is too long to train the models. There are a couple of reasons why it might be necessary to continue training for this long. Firstly, it is always possible for a model to find a new local minimum in its parameter space, and so ending the training process early risks missing out on a model with a potentially lower loss. Secondly, only the model with the lowest loss is kept as the final model, meaning, as long as overfitting is not occurring, there is no harm in letting the model continue training once it has seemingly converged. Thus a training length of 100 epochs is justified in this case.

2.3.2 Copyright

The online abstract of this publication is accessible at `https://doi.org/10.1364/OE.443932`.

3 Deep learning for multi-point fibre temperature sensing

3.1 Introduction

Temperature sensing with optical fibres is traditionally done through two main methods; sensing with a wavelength spectrum, such as fibre Bragg gratings (FBGs), and scattering based sensing, such as using optical time-domain reflectometry (OTDR). Scattering based sensing methods can be truly distributed, while there are methods for performing multi-point sensing using the wavelength spectrum. Like the vast majority of fibre applications, silica fibres are generally used for temperature sensing. Due to its softening point, sensing with silica fibre is not possible above 1300℃ [67]. The leading alternative for fibre temperature sensing above this temperature is sapphire crystal optical fibre. A sapphire fibre temperature sensor with a femto-second laser written FBG has been shown to function up to 1900℃ [68]. Sapphire fibre however carries its own limitations, such as a high number of supported modes, resulting in broad FBG peaks which reduce sensing resolution and multiplexing capabilities. This motivates the need for alternative methods of analysing sapphire fibre wavelength spectra for high temperature sensing, the method being explored in this chapter being deep learning.

Resonance-producing structures such as fibre Bragg gratings (FBGs) and Fabry-Perot interferometers (FPIs) are built into optical fibres so that sensing may be performed using the resulting wavelength interference spectrum [4] (this was discussed in more detail in Section 1.1). Such structures encode information in the wavelength spectrum that is easy to track and correlate with an environmental parameter; for FBGs this is a resonant peak and for FPIs this is a periodic feature, who's periodicity in the frequency domain is referred to as the free spectral range (FSR). In the case of FBGs, the shift in a resonant wavelength is extracted for sensing, while for FPIs it is the phase, which is also a wavelength shift but of the whole periodic spectrum.

Multi-point sensing is achieved with FBGs via wavelength division multiplexing (WDM). This involves inscribing FBGs of differing resonant wavelengths such that the information pertaining to the different structures may coexist in the wavelength spectrum and the useful information from each extracted separately. There are a number of issues with this method however. Structures such as FBGs can be costly and time consuming to inscribe in an optical fibre. Sensing is also limited by the bandwidth of the source as well as the spectrum analyser. Furthermore, such sensors will always suffer from cross-sensitivity against environmental parameters not being sensed. In the case of multimode FBGs, bandwidth resolution is further hindered by the broadening of resonant peaks due to the multiple present modes [69].As mentioned above, sensing with traditional silica fibre is also not possible at high temperatures.

Recent attention has been paid to the use of machine learning for optical fibre sensing, which holds promise to increase sensitivity and reduce cross-sensitivity. Nguyen et al. [62] demonstrated the extraction of single-point temperature information from the transmission wavelength spectrum of sapphire crystal optical fibre by training a deep neural network on these wavelength spectra, each with an associated temperature label [62]. This fibre was unaltered and had not had any resonance-producing structures built into it. This work also showed noise immunity by deliberately shaking the fibre such that the recorded spectra's response to this noise far outweighed that of temperature changes. These spectra were used to train a multi-layer perceptron DNN, and it was shown that this DNN was still able to effectively learn and predict the relationship between the heavily noise-affected spectra and the temperature under which they were recorded. This demonstrated the deep learning approach's robustness against cross-sensitivity to unwanted environmental parameters affecting the fibre being used. Conventional sensing techniques in the presence of multiple parameters which affect the fibre output are unable to distinguish the individual effects without calculating cross-sensitivities between each parameter, for example

temperature and pressure [70]. Nguyen et al. have shown that deep learning techniques are able to extract information from the output of an MMF pertaining to a single environmental parameter without prior knowledge of its cross-sensitivity with other parameters.

This chapter presents work which is an extension of [62], in which DNNs are trained for multi-point temperature sensing at 10 discrete, spatially resolved points using the wavelength spectra from a variety of fibres. It is demonstrated that the network trained on sapphire fibre wavelength spectra performs far more accurate multi-point sensing than those trained on the spectra from more conventional fibres. This is attributed to the mode coupling induced by the fluctuating fibre diameter and hence fluctuating number of supported modes along the length of the sapphire fibre. We show using numerically modelled results that the mode mixing due to a variable radius can give an optical fibre sensor inherent distributed sensing capabilities.

3.2 Theory and numerical modelling

3.2.1 The wavelength spectrum and spatially resolved information

A local perturbation on a fibre, such as heating, will create a local change in fibre's refractive index, and hence a different set of supported modes for the length of this perturbation. This will cause the propagating electromagnetic power to couple into the new set of modes for the duration of the perturbation, before coupling back into the original set. As the optical fibre transmission is linear, perturbations in various positions are expected to have the same effect on the resulting optical fibre output.

A consequence of this is that the wavelength spectrum from a perfectly translationally invariant fibre should hold no information about where a perturbation has taken place along the fibre, rather it is the culmination of the effects of all the perturbations that exist along the fibre. In order

to gain distributed information in a translationally invariant fibre then the symmetry of the system needs to be broken, such as with FBGs or FPIs.

Sapphire crystal optical fibre (SOF) fibres are grown in the desired shape of a fibre, unlike glass silica fibres, which are drawn from a preform. This process is much less precise than drawing a preform, leading to an fibre diameter which varies with length. The diameter in fact varies between 60μm and 80μm over distances on the order of millimetres. A consequence of this is that the number and nature of the supported modes in the fibre will vary with the fibre's length, meaning the modal distribution of power will constantly need to be redistributed as the set of supported modes in one section of fibre couples into the set in the next. Although it is possible to induce mode mixing in otherwise translationally invariant fibre through bending, the mode mixing in sapphire fibre will be almost continuous and unique as the fibre diameter changes almost arbitrarily.

3.2.2 Theory of mode coupling

This section aims to provide numerical evidence that spatial perturbations in a fibre, specifically diameter changes, are required to provide the symmetry breaking that is needed for discrimination of spatially separated sensing events in a MMF. A consequence of this will be evidence that sapphire crystal optical fibre is a suitable candidate for distributed sensing when paired with deep learning techniques.

Eq. 17 described the light in a MMF as the superposition of orthogonal modes. The distribution of the total power transmitted through a fibre between these modes is given by the modal coefficients a_j, the relative weighting between the modes. The specific distribution is dependent upon the launching conditions of light into the fibre. Unless specific effort is made to launch light into higher order modes, it is the lower order modes which tend to carry more power.

When the light in a MMF is incident on a section of fibre with different

supported modes, i.e. two different fibres spliced together or simply a perturbation in the radius or refractive index of a single fibre, the total power will be redistributed amongst the new set of modes. This new distribution is dependent on the original modal coefficients and the amplitude overlap integrals between each pair of old and new modes.

For light coupling between two sections of fibre with differing modal solutions, continuity of the transverse electromagnetic field at the interface between these sections gives

$$\sum_j a_j \hat{\mathbf{e}}_{tj} - \sum_j b_j \hat{\mathbf{e}}_{tj} = \sum_j c_\nu \hat{\mathbf{e}}_{t\nu} \tag{22}$$

$$\sum_j a_j \hat{\mathbf{h}}_{tj} - \sum_j b_j \hat{\mathbf{h}}_{tj} = \sum_j c_\nu \hat{\mathbf{h}}_{t\nu}, \tag{23}$$

where $\hat{\mathbf{e}_{tj}}$ and $\hat{\mathbf{h}_{tj}}$ represent the transverse electric and magnetic modal fields of the jth supported mode in the first fibre, $\mathbf{e}_{t\nu}$ and $\mathbf{h}_{t\nu}$ represent those of the ν^{th} supported mode of the second fibre, a_j represents the modal coefficient of the jth incident mode in the first fibre, b_j represents that of the jth reflected mode in the first fibre and c_ν that of the ν^{th} transmitted mode in the second fibre. It is assumed that a_j are a result of the coupling of the light into the fibre and are already known, which leaves b_j and c_ν to be solved for. By taking the right cross product of Eq.(22) with $\hat{\mathbf{h}_\nu^*}$ and the left cross product of Eq.(23) with $\hat{\mathbf{e}_j^*}$ and exploiting the orthonormality of modes, one obtains

$$c_\nu = \frac{1}{2}\left(\sum_j a_j \int_{A_\infty} \hat{\mathbf{e}_j} \times \hat{\mathbf{h}_\nu^*} \cdot \hat{\mathbf{z}} dA + \sum_j b_j \int_{A_\infty} \hat{\mathbf{e}_j} \times \hat{\mathbf{h}_\nu^*} \cdot \hat{\mathbf{z}} dA\right) \tag{24}$$

$$c_\nu = \frac{1}{2}\left(\sum_j a_j \int_{A_\infty} \hat{\mathbf{e}_\nu^*} \times \hat{\mathbf{h}_j} \cdot \hat{\mathbf{z}} dA - \sum_j b_j \int_{A_\infty} \hat{\mathbf{e}_\nu^*} \times \hat{\mathbf{h}_j} \cdot \hat{\mathbf{z}} dA\right). \tag{25}$$

Eqs.(24) and (25) are most easily solved in matrix form. By defining the vectors

$$\mathbf{a} = [a_1, a_2, ...a_j...] \tag{26}$$

$$\mathbf{b} = [b_1, b_2, ...b_j...] \tag{27}$$

$$\mathbf{c} = [c_1, c_2, ...c_\nu...], \tag{28}$$

and the matrices

$$M_{j\nu} = \frac{1}{2}\int_{A_\infty} \hat{\mathbf{e}_\nu^*} \times \hat{\mathbf{h}_j} \cdot \hat{\mathbf{z}} dA \tag{29}$$

$$N_{j\nu} = \frac{1}{2}\int_{A_\infty} \hat{\mathbf{e}_j} \times \hat{\mathbf{h}_\nu^*} \cdot \hat{\mathbf{z}} dA, \tag{30}$$

and using the Equations 24 and 25 to eliminate $\mathbf{b}$, one obtains Eq.(31), an expression for $\mathbf{c}$, the modal distribution of power in the second fibre, in terms of $\mathbf{a}$ [71].

$$\mathbf{c} = 2\mathbf{a}\left(N^{-1} + M^{-1}\right)^{-1}. \tag{31}$$

While the mode coupling conditions at the join between two fibres can be solved analytically, solutions for more arbitrary fibre perturbations such as a continually varying fibre radius or refractive index are more difficult to solve for, and rely on approximations such as the weak guidance and slow varying approximations [6].

3.2.3 Numerically modelled results

Numerical modelling of the transmission of light through a system of two adjacent fibres and the coupling of modes between them was undertaken. A program was written in Matlab [72] to solve for the modes in two sections of fibre, as in Section 1.1.2, and compute the coupling of light from one to the other as per the analysis above. The refractive index of the fibres was

changed as according to a thermo-optic coefficient of 1.1×10^{-5} T^{-1} [73]. A specklegram intensity pattern at the end facet of the second fibre was then generated, with the goal of investigating spatially resolved information pertaining to the two sections of fibre from this output.

A specklegram output was chosen as opposed to a wavelength spectrum as the computational time needed to produce a specklegram with the program used was orders of magnitude less. A specklegram is effectively produced for each individual point of a wavelength spectrum in order to calculate the transmitted intensity, hence a spectrum containing 1000 points (as did the spectra recorded in the experimental section of this chapter) will take 1000 times longer to produce than a specklegram output. Despite their inherent differences, both should contain spatially resolved information, should it exist, due to continuous mode coupling in the fibre, and the results drawn from one will generally be applicable to the other.

The specklegram output of the fibre simulation was used to investigate means of encoding spatially resolved information pertaining to the two sections of fibre in such an output, such that the information could be learnt by a DNN. Two possible mechanisms by which this could occur were investigated; mode mixing due to a variable fibre radius, and a mode-dependent loss in the fibres, with higher order modes being more lossy than lower order modes.

In order to test the effectiveness of these two mechanisms in distinguishing the spatial position of otherwise identical perturbations on a fibre, two specklegrams were generated for each applied mechanism, one with the first section of fibre at 25℃ and the second at 50℃, and vice versa. To evaluate and quantify the differences between the generated specklegrams a zero-normalised cross correlation function between the two specklegrams was used. This is defined as

	First fibre heated	Second fibre heated	ZNCC score
Control	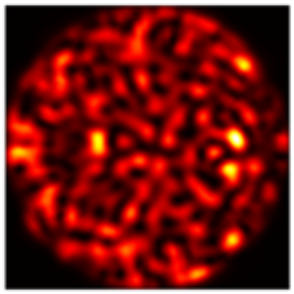	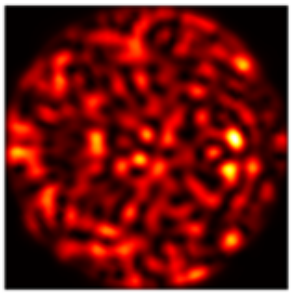	0.9798
Mode dependent loss	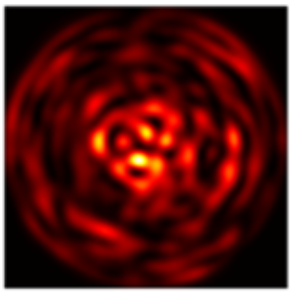	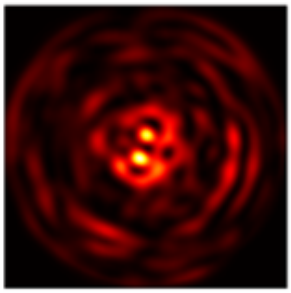	0.9188
Radius mismatch (22µm-18µm)	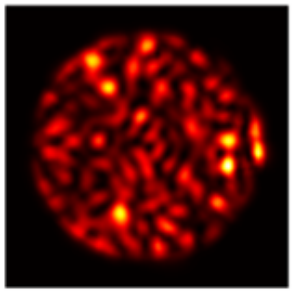	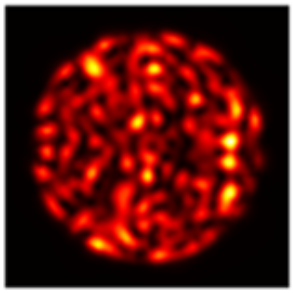	0.7261
Radius mismatch (18µm-22µm)	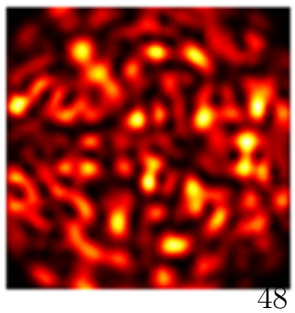	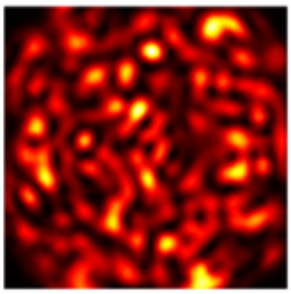	0.4345

Figure 9: Specklegrams generated under no additional assumptions, the assumption of mode dependent loss, and two instances of a fibre radius disjoint. The two specklegrams were generated with the two sections of the fibre at 25℃ and 50℃ and vice-versa. The ZNCC score represents the correlation score between the two specklegrams.

$$Z(I_1, I_2) = \frac{\sum_N (I_1 - \bar{I}_1)(I_2 - \bar{I}_2)}{[\sum_N (I_1 - \bar{I}_1)^2 \sum_N (I_2 - \bar{I}_2)^2]^{\frac{1}{2}}}, \tag{32}$$

where I_1 and I_2 denote the pixel intensity of two images, N denotes the pixels in the images to be summed over and the barred intensities denote the average intensity of the image. The ZNCC theoretically returns a value between -1 and 1, but unless images are specifically negatively correlated, the value will generally lie between 0 and 1, with 0 denoting no correlation between the images, and 1 denoting the images as positively correlated

Figure 9 displays the two specklegrams generated under each set of assumptions, as well as the ZNCC score between them. In all circumstances, the two sections of fibre were chosen to be 15 cm long, with $n_{co} = 1.45$, $n_{cl} = 1.40$ and $\lambda = 1.55\,\mu m$. The fibre was chosen to be 20 μm in radius, with the radius mismatch mechanism being achieved with fibres of section radii 19 and 21 μm and 18 and 22 μm. The "control" was carried out with the ideal propagation of light through the fibres in the absence of any other mechanisms. The "mode dependent loss" was simulated by assigning each calculated mode an extinction coefficient, κ, from a linear distribution of values, assigning the lowest extinction coefficients to the lowest order modes. The extinction coefficient represents an imaginary component of each mode's effective refractive index, such that Eq. 19 becomes

$$\beta = \frac{2\pi}{\lambda}(n_{eff} - i\kappa). \tag{33}$$

The "radius mismatch" model was performed twice, with the diameters in the first and second fibre being 18μm-22μm and 22μm-18μm for the two cases

The results of the "control" reflect what was discussed in Section 3.2.1, in that in the case of ideal multimode fibre transmission, the effect of a

perturbation on the output of the MMF is independent of the translational position of the perturbation. This is reflected in the ZNCC score close to 1, showing the two outputs corresponding to the two spatially resolved perturbations being very similar.

The largest difference in specklegrams comes from the "radius mismatch" cases as opposed to mode dependent loss, giving evidence that the induced mode mixing due to a change in fibre radius is able to give evidence about the spatial position of a perturbation along a fibre. The effect appears to be greatest when the higher-moded fibre is producing the specklegram, but both cases produce significantly more different specklegrams than the two cases with a constant fibre radius.

Despite the apparent existence of this spatially resolved information, it is only useful if it is able to be extracted using a method of analysis. For this work, this method is by using a deep neural network (DNN). To this end, 50 specklegrams for each of the control, mode dependent loss and radius mismatch cases were generated, each with a random temperature between 25℃ and 50℃ in each of the two fibre sections. The specklegrams and temperature labels were used to train a DNN with the goal of overfitting to the small set of data. In the absence of a large set of data (due to the time constraints of generating these specklegrams), the ability to overfit to this dataset is the best indication of the existence of a physical function between the specklegrams and temperature labels. In this case, it is sufficient to demonstrate this overfitting ability, rather than demonstrate generalisation capabilities, to make conclusions about distributed temperature information in the fibre's output. In the case of overfitting, one also expects the validation loss to be high, as the trained model will lack generalisation capabilities.

Multilayer perceptron networks with four hidden layers were fed the 150×150 pixel specklegrams and trained for 250 epochs. A mean squared error loss function between the true temperature labels and those predicted by the DNNs was used for training. The results in Table 1 make it obvious

	Training loss (℃)	Validation loss (℃)
Control	0.65	20
Mode dependent loss	0.68	8.8
Radius mismatch	0.089	0.52

Table 1: Training and validation loss between the true and predicted temperature labels corresponding to the specklegrams after 250 epochs of training. It is the overall loss pertaining to predictions on two temperature labels, and so is the average between them.

that the DNN trained on specklegrams generated with a mismatch in radius between the two fibre segments was able to find a learnable connection in the data much easier than the other two cases. This indicates that the mode mixing due to a change in fibre radius is able to encode spatially resolved information in a MMF output that is not there when the such strong mode mixing is not induced.

3.3 Experimental design and data collection

The aim of this experiment was to test experimentally a DNN's ability to learn and perform multi-point fibre temperature sensing using the wavelength reflection spectra collected from different fibres including sapphire fibre. These wavelength spectra were collected while the fibres lay inside of a furnace, with ten temperature labels simultaneously recorded, such that DNNs could be trained for temperature sensing with this data. As well as seeing in general the possibility of multi-point regression-based sensing using a DNN, the results from the sapphire fibre will give insight into the idea of continuous mode mixing leading to spatially resolved information in the output of an MMF, as explored numerically earlier in the chapter.

Although the theory earlier in this chapter uses the specklegram output of a multimode fibre, a wavelength spectrum was chosen to be recorded for this experiment due to the ease of experimental setup in this situation. As the furnace used had one entry point, the reflected light from the fibre's end facet was interrogated, something which would be difficult to record the

specklegram of. Both forms of MMF output however will carry the complex, spatially-resolved information required for the multi-point sensing.

Reflection wavelength spectra from the fibres was collected under different temperature distributions, thus providing a variety of temperature labels for each individual sensing point. The temperature distributions were achieved by placing the fibres in various positions relative to a furnace. Spectra were collected using a swept-source interrogator, an instrument which sends and receives a coherent light source at a range of wavelengths, measuring the intensity of light received at each wavelength and displaying this as a power spectrum in the wavelength domain.

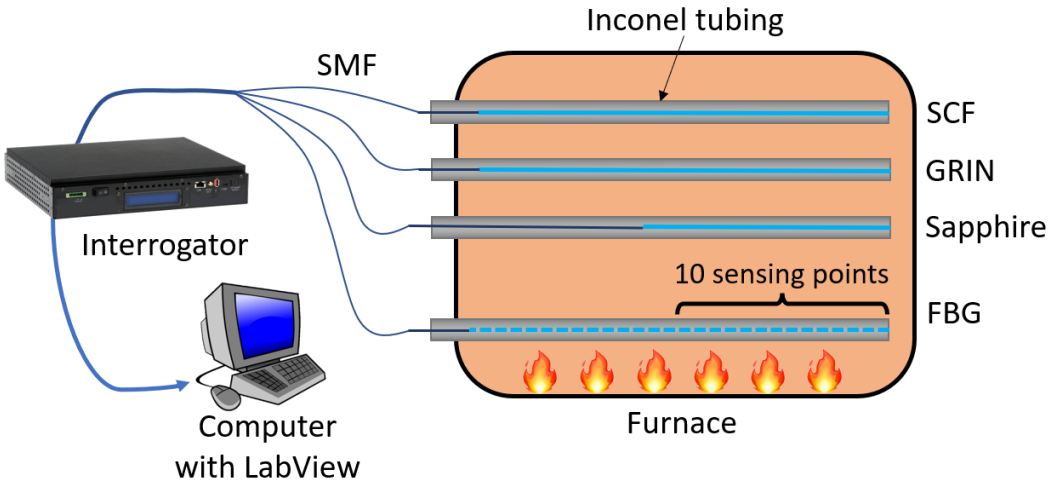

Figure 10: Experimental setup.

The three fibres used for this experiment were sapphire crystal optical fibre (SOF) purchased from Micromaterials, in-house fabricated silica suspended core fibre (SCF) [74] and silica graded index fibre (GRIN) purchased from Nufern. The two silica fibres were prepared for high temperatures by stripping their coatings using fibre strippers. As it was reflection spectra being recorded for the experiment, the end facets of the fibres needed to be flat to reflect enough light intensity to be recorded by the interrogator. For the silica fibres, this could be achieved with a fibre cleaver. The sapphire fibre however can not be cleaved using a conventional cleaver

as the crystal structure will not allow for a flat surface to be produced in this fashion. For that reason, the sapphire fibre was additionally polished using a fibre polisher to ensure a flat end facet capable of creating a measurable reflected signal. The end of the sapphire fibre spliced to the single mode fibre was also intentionally made non-flat, so as to nullify the reflection signal from this interface being picked up by the interrogator. This was done as the sapphire fibre is very lossy, and this reflection signal would overpower that of the end facet reflection. A 15cm length of sapphire was used, while 25cm lengths of SCF and GRIN were used.

The fibres were packaged in inconel tubing to protect from impurities present in the furnace air, before being spliced to single mode fibre using a Fitel s179a fusion arc splicer. The single mode fibre was similarly spliced to a single mode optical patch cable, which was connected to a 1460-1620 nm Micron Optics Hyperion si255 swept source interrogator to produce a reflection spectrum.

To collect the multiple temperature labels that the DNNs would be learning to predict, 10 points of a 20-point fibre Bragg grating (FBG) were used. An FBG was chosen over other temperature sensing methods such as thermocouples as it was by far the easiest method of achieving 10 sensing points. The particular FBG used was fabricated by inscribing 10 Bragg gratings in suspended core fibre using a femto-second ablation laser [75]. The FBG was prepared similarly to and bundled with the fibres above.

Once packaged, all four tubes containing the fibres were bundled together such that the end facets of the fibres coincided. This bundle was kept together throughout the entirety of the data collection. The 10 Bragg gratings consisting the 10 sensing points began a few millimetres from the end of the FBG fibre, and were spaced every 1.5 cm. Only 10 sensing points were used as it was only these 10 which lay adjacent to all three sensing fibres, given the length of sapphire used was 15 cm.

Data was collected over 11 separate 24 hour periods, with the fibres in

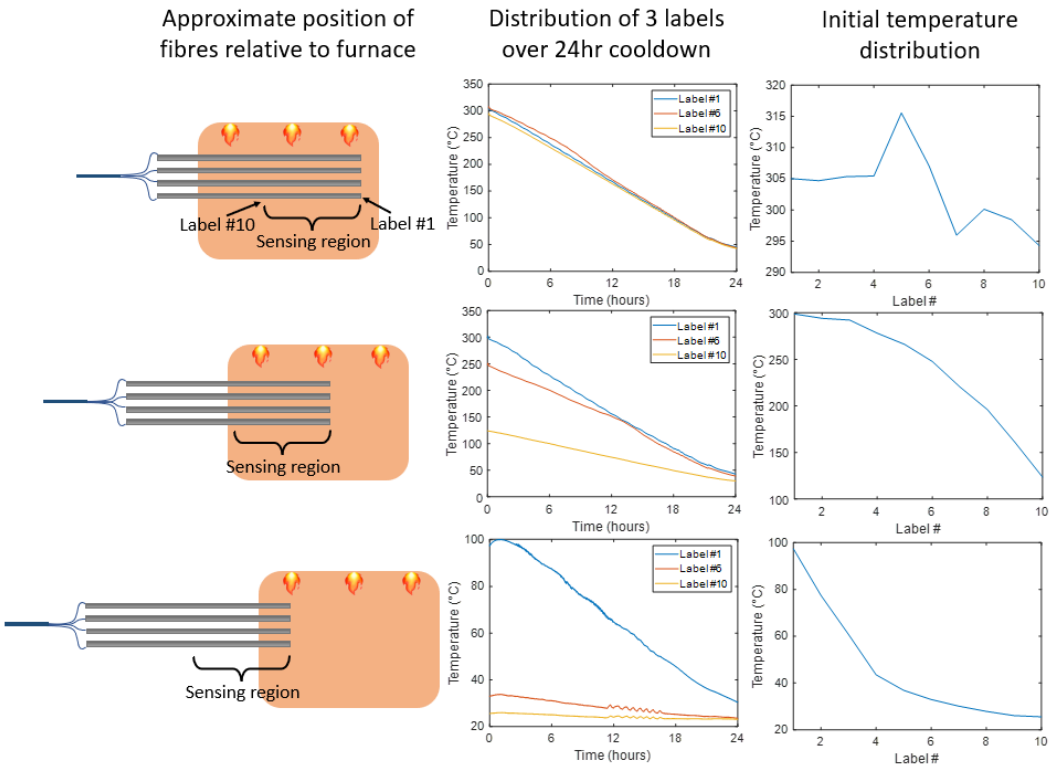

Figure 11: Examples of the positions of the fibres used relative to the furnace, the resulting temperature progression of the outermost labels and one in the middle, and the initial temperature distributions when the furnace was at its hottest.

a different spatial position relative to the furnace for each. The furnace was let to cool linearly from 300℃ to 25℃ over these periods, such that each spectrum recorded was under a unique temperature distribution, and each sensing point experienced an independent variety of temperature labels. Examples of these distributions and an approximate positioning of the fibres that created them are shown in Figure 11.

Of these 11 sets of data, each containing 72,000 spectra, six were combined to train the networks, with the performance of each evaluated using the testing dataset, and the remaining five were used to test the networks' generalisation capabilities. The six sensor positions comprising the training data were spaced equidistant, beginning with the sensors placed

as far inside the furnace as possible, and finishing with the sensors' end facets close to the exit of the furnace. The five positions used to test the networks' generalisation capabilities each lay between a pair of these six positions, in a quasi-random position between the two.

Wavelength spectrum data was read in from the interrogator to a LabView program. Examples of the spectra obtained from each of the fibres is shown in Figure 12. The raw spectra contained 20,000 data points, with a resolution of 8 pm. All spectra were decimated by a factor of 20, resulting in 1,000 point spectra with a resolution of 0.16 nm. This was done to reduce memory usage on the recording computer as well as save computational power while training the DNN.

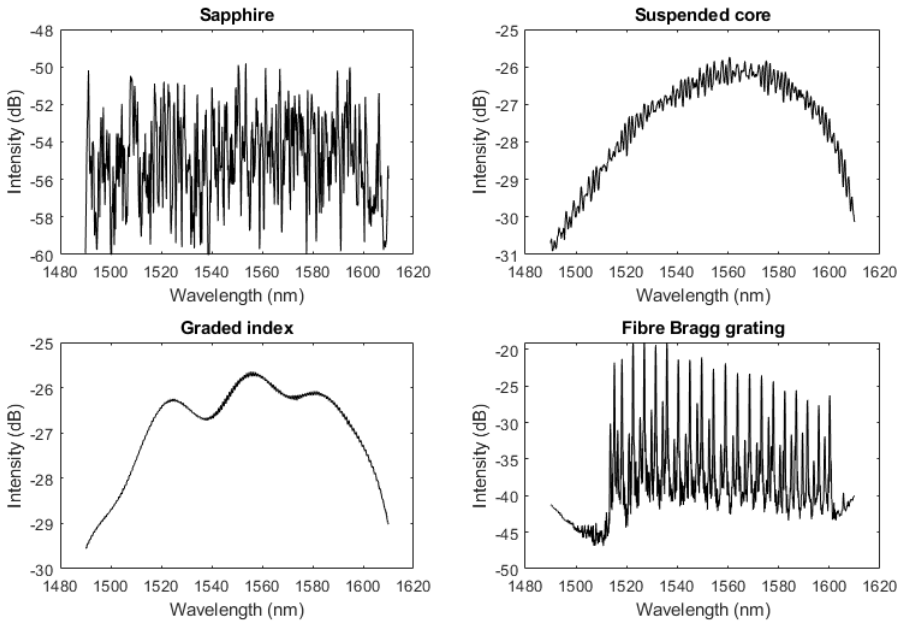

Figure 12: Example wavelength reflection spectra obtained from the four fibres

The FBG sensor consisted of 20 gratings, spaced 1.5 cm apart and resonant peaks spaced approximately 5 nm apart in the wavelength domain. Temperature labels for each grating were obtained using a peak tracking algorithm implemented in Matlab [72] and a calibration curve relating the

shift in resonant peak to the change in temperature experience by the FBG. This calibration curve had been experimentally obtained by the group that designed the fibre using a fourth order polynomial fit:

$$\Delta T = a_1 \left(\frac{\Delta\lambda}{\lambda_{RT}}\right) + a_2 \left(\frac{\Delta\lambda}{\lambda_{RT}}\right)^2 + a_3 \left(\frac{\Delta\lambda}{\lambda_{RT}}\right)^3 + a_4 \left(\frac{\Delta\lambda}{\lambda_{RT}}\right)^4, \tag{34}$$

where ΔT denotes the shift in temperature from room temperature in ℃, $\Delta\lambda$ denotes the shift in peak wavelength from the peak room temperature wavelength, and λ_{RT} denotes the room temperature wavelength. The coefficients, a_i have been determined as

$$a_1 = 1.516068 \times 10^5 \,℃ \tag{35}$$

$$a_2 = -1.387818 \times 10^7 \,℃ \tag{36}$$

$$a_3 = 1.874080 \times 10^9 \,℃ \tag{37}$$

$$a_4 = -1.060863 \times 10^{11} \,℃. \tag{38}$$

3.3.1 Deep learning

The DNN architecture used in this analysis was a multi-layer perceptron with an input layer of the 1,000 point spectra, output layer corresponding to the 10 temperature labels, and four hidden layers of size 512, 128, 64 and 32. Figure 13 gives a representation of this MLP architecture. The 432,000 spectra comprising the dataset were shuffled and split into training, validation and testing sets, the proportional size of each being 67.5%, 22.5% and 10% of the total dataset respectively. Training was implemented using the Keras library. For the 360,000 spectra from the five sets of data intended to test the networks' generalisation capabilities, separate from the training data, these were not split into three groups, as they were not needed for training, and none had been seen by the networks during the course of this

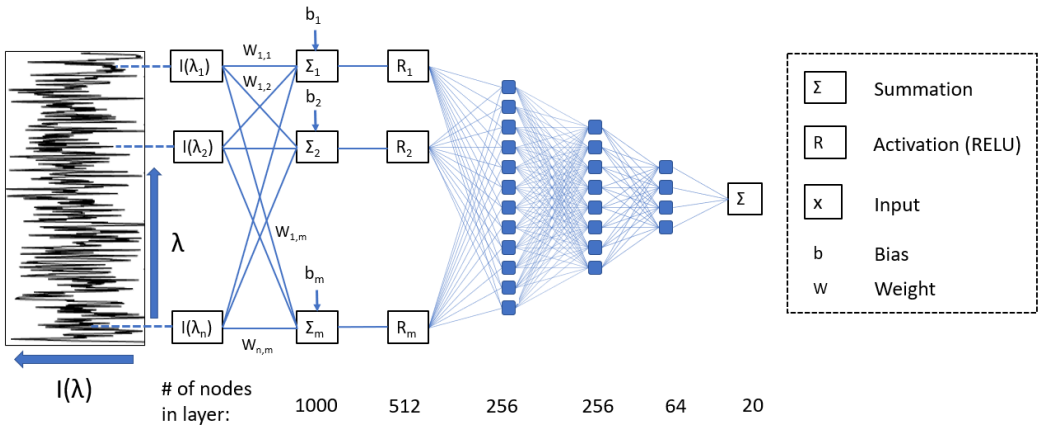

Figure 13: Representation of the deep neural used in this analysis. It consisted of four hidden layers, with the number of nodes in each shown in the figure

work. All of these spectra were instead used purely for testing in Section 3.4.2 with the models trained in this section.

The optimisation algorithm used for training was the Adam optimiser [76]. Hyperparameters included a learning rate of 10^{-3}, batch sizes of 64 and a training length of 500 epochs. The model with the lowest loss that was created during training was kept as the final model. Training was performed on a Lenovo Legion 7i laptop with a 10th Gen Intel Core i7-10875H processor, 16 GB of memory and an NVIDIA GeForce RTX 2070 graphics card. Training over 500 epochs took approximately two hours.

3.4 Results

3.4.1 Training and testing within the dataset

The models were trained on the 291,600 spectra (67.5% of the 432,000 spectra), and the performance of the networks was tested using the set of 43,200 testing spectra (10% of the 432,000 spectra). These had not been seen by the network during training. The training was performed with a 'model checkpoint' in place, which only saved a particular model resulting from an epoch as the new model if the loss at the end of this epoch improved on that

of the current best model.

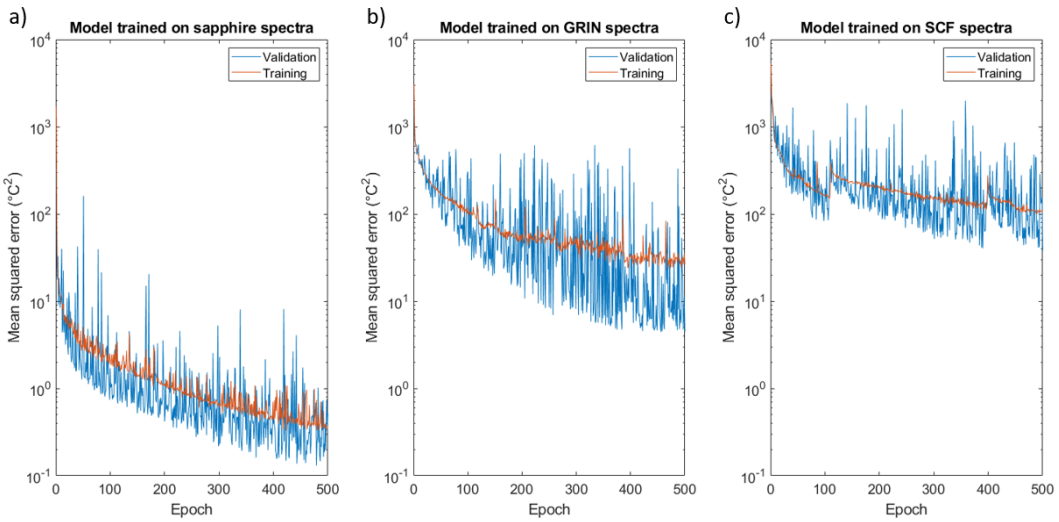

Figure 14: The loss history for the 500 epochs of training performed on the models using spectra from a) sapphire fibre, b) graded-index fibre and c) suspended core fibre

Figure 14 shows the history of the MSE loss at the end of each 500 training epochs for the training process of the three models. Each plot has the same y-axis scale. From these plots, one can draw two conclusions. First of all, it appears that each model was still slightly improving at the end of the 500 epochs, leading one to believe the models were not done training. This is exaggerated however by the logarithmic y-axis, and it can safely be said that further training would not have worthfully improved the models. Secondly, it is obvious that the model trained on the sapphire fibre spectra reached a much lower loss value than that of the GRIN fibre, which in turn reached a much lower loss value than that of the SCF fibre. This indicates that there is a clear distinction between the ability for the DNN architecture employed to find a meaningful connection between the spectra and 10 temperature labels between the three fibres, with the model learning best with the sapphire spectra and worst with the SCF spectra.

The results pertaining to the performance of the three models are presented in the form of a root-mean-squared error metric between the 10

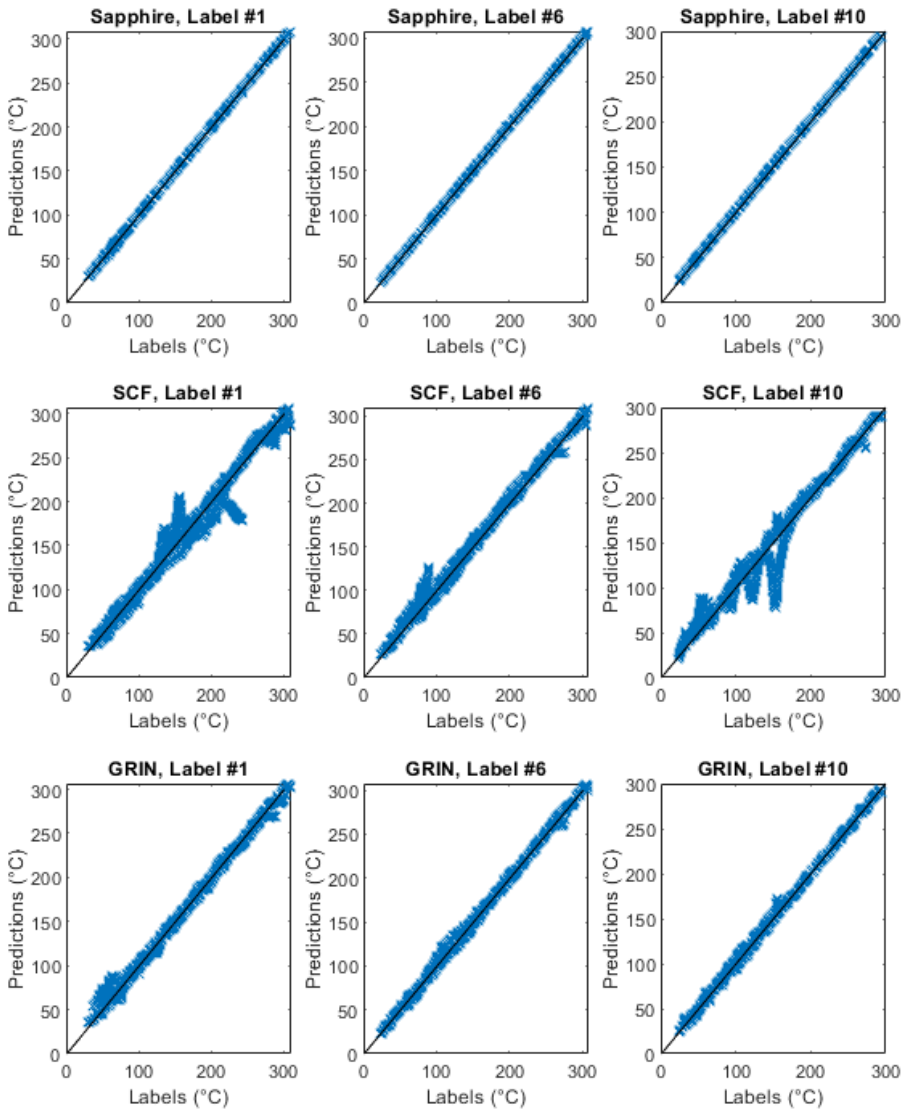

Figure 15: Predictions of the three DNNs on three selected temperature sensing positions out of the 10 they were trained on.

Fibre	Label#1	Label#2	Label#3	Label#4	Label#5
Sapphire	0.83	0.64	0.56	0.42	0.38
GRIN	5.0	3.4	2.9	2.9	2.9
SCF	9.6	7.6	6.8	6.1	5.7

Fibre	Label#6	Label#7	Label#8	Label#9	Label#10
Sapphire	0.48	0.55	0.53	0.65	0.84
GRIN	2.5	2.0	1.8	1.8	2.4
SCF	6.1	7.0	7.3	8.0	9.3

Table 2: RMS error (°C) of predictions made by the networks trained on data from the three fibres for each of the 10 sensing points.

temperature labels predicted by the networks when given a test spectra, and the 10 true temperature labels. The labels start with label #1 at the end of the fibres, closest to their end facets, and count up, with label #10 being furthest from the end facet. Table 2 displays this RMS error for the DNNs trained on the data from the three fibres in predicting the 10 distributed temperature labels from the testing dataset.

Figure 15 shows examples of the predictions on three of the 20 temperature labels, showing more explicitly how the DNNs performed with individual sensing points. From the results displayed, it is clear that the DNN trained on sapphire fibre spectra is by far the most accurate model in predicting each of the 10 temperature labels corresponding to a spectrum and temperature distribution not seen during training. This is supported by the low loss achieved by the model during training, which is two orders of magnitude lower than the next model, suggesting a meaningful and physical relationship between the sapphire fibre spectra and the spatially resolved temperature measurements. It is also supported by the high accuracy of the model, again up to to an order of magnitude more accurate than the other two models.

It is hypothesised and experimentally supported here that the sapphire fibre, with its variable radius and hence constant mode mixing, is more

Fibre	Label#1	Label#2	Label#3	Label#4	Label#5
Sapphire	15	11	8.9	6.0	4.9
GRIN	21	19	17	14	11
SCF	15	12	9.9	7.9	7.7

Fibre	Label#6	Label#7	Label#8	Label#9	Label#10
Sapphire	5.2	5.8	6.4	5.4	5.1
GRIN	10	9.5	8.6	8.0	9.5
SCF	8.9	11	13	13	14

Table 3: RMS error (°C) of predictions made by the networks trained on data from the three fibres for each of the 10 sensing points.

capable of distributed sensing using its wavelength spectrum than an ordinary fibre which does not possess this characteristic. This is due to the unique contribution to the output of the fibre from each spatially resolved point along the fibre due to the unique mode mixing occurring at that location, as opposed to contributions from each point along the fibre being summed up equally.

3.4.2 Generalisation to unseen temperature distributions

The second part of this experiment was to test the trained models' ability to generalise to temperature distributions they had not seen during training. This was achieved by collecting data as mentioned earlier in this section, which involved sets of data from sensor positions which did not go into the set of training data. In general it is not expected that DNNs should be able to generalise to data which sits completely outside of the distribution of data which comprised its training set. This includes similar data which has simply been recorded under slightly different conditions or methods, intentional or not. As such, it is not expected that the models trained in this experiment will perform to a similar standard as the previous section, but conclusions can still be drawn by comparing the performance of the three models in attempting this task.

The generalisation capabilities of the trained models were tested on 360,000 spectra from five sensor positions which the model had not seen during training. Each of these positions lay between The 360,000 spectra were all handled in the same way as the training data, i.e. normalised. The spectra were then fed into the models trained in Section 3.4.1 and predictions on the 10 training labels made.

Table 3 and Figure 16 display the results of the predictions and the accuracy of the three models as in Section 3.4.1. The first thing to note is that the models are far less accurate at predicting the temperature labels from spectra which were generated from different temperature distributions than those which comprised the training set. The model trained on the sapphire fibre's spectra is slightly more accurate, but not significantly.

One possible reason the performance of the three models is overall inaccurate is the changing polarisation state of the light travelling through the fibre when the single mode optical patch cables leading to and from the interrogator are perturbed. This occurs when the sensors' positions are shifted and can have a profound effect on the spectrum recorded by the interrogator in the absence of any other perturbations. Figure 17 shows two example spectra from a GRIN fibre sensor, where the only perturbation applied was manual movement of the optical patch cables leading to and from the interrogator.

A consequence of this is that it is not only the temperature distribution surrounding the fibre which affects the wavelength spectrum, but in this case the position of the SMF patch cables used and hence the polarisation state of the light. In reality there are countless environmental variables which affect the recorded spectrum and the performance of the DNNs, everything from atmospheric pressure to the calibration of the interrogator and even the random seed selected in the code used for training the models. DNNs prove themselves to be very powerful at learning the required relationship between the x- and y-data it is presented with, in this case wavelength spectra

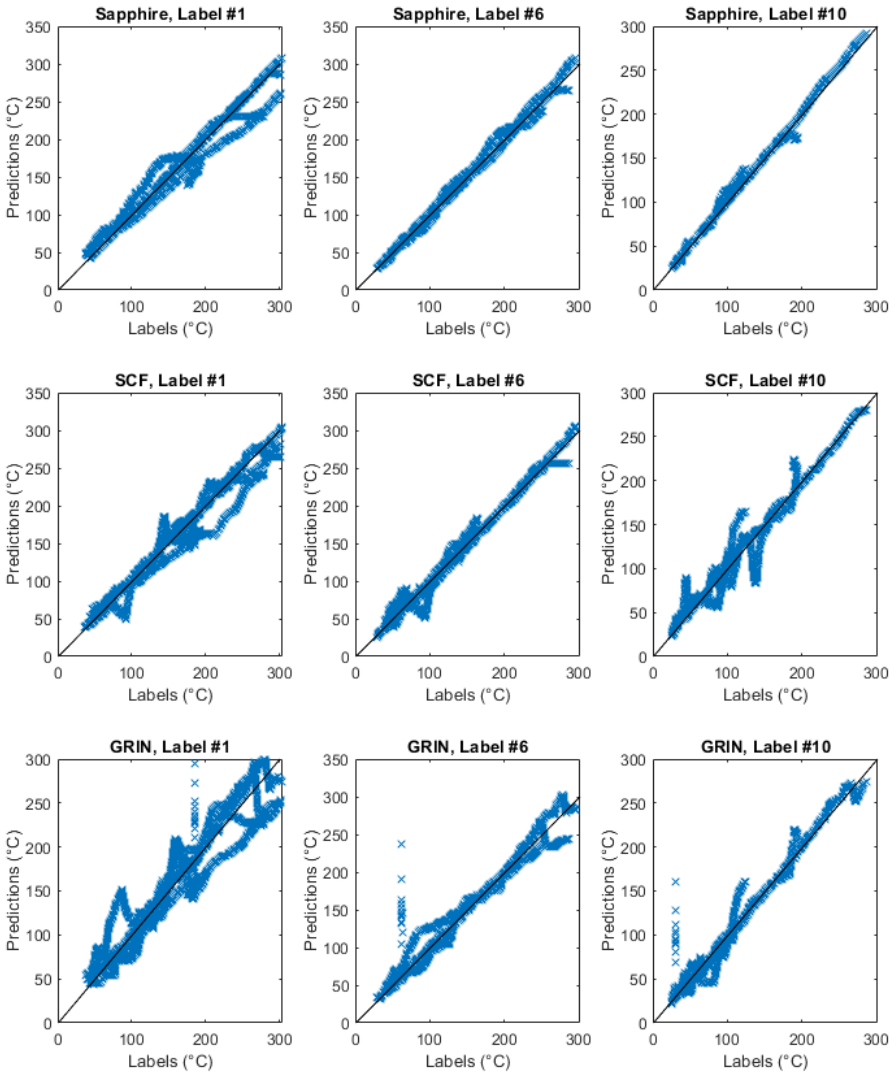

Figure 16: Predictions of the three DNNs on three separate temperature labels for the unseen temperature distributions

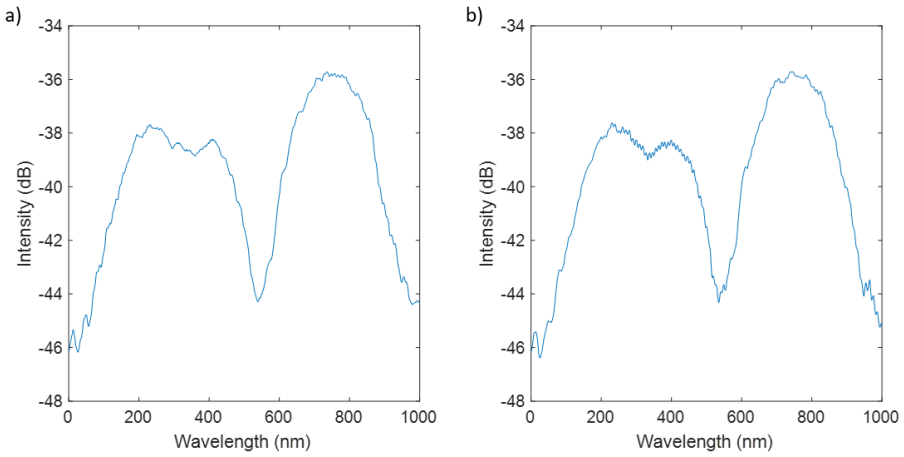

Figure 17: Two wavelength spectra, a) and b), recorded from the same graded-index fibre sensor seconds apart. The fibre itself was held still and the only perturbation applied was movement of the single mode optical patch cable leading to and from the interrogator

and temperature labels, and learning to ignore/see through other parameters which affect the y-data, such as mechanical noise in the case of [62]. However, they are only capable of doing this when they are shown many examples of the full extent of this noise, and consequently how its effects on the y-data are not due to the x-data. In our case, data relating to each sensor position is recorded for 24 hours with the patch cables in the same position, and hence the DNNs are unable to learn the effect of patch cable position on the wavelength spectrum. The effect on the spectra from the different patch cable positions for the datasets not seen during training is then attributed to a temperature change, and the DNNs perform poorly.

A possible solution to this is to use polarisation maintaining single mode fibre patch cables, such that perturbations on the patch cables will not have an effect on the spectra, which is a subject for future work. It is hypothesised however that using the polarisation maintaining single mode fibre and patch cables will improve the DNNs ability to generalise to unseen temperature distributions.

3.5 Conclusion and future work

The experimental results presented here demonstrate that a DNN trained on wavelength spectra for temperature sensing from a fibre with variable radius, such as sapphire fibre, is far more likely to be able to discern spatially resolved information than those trained on data from other fibres. Together with the numerically modelled results, this gives evidence that a fibre with a variable radius, or more generally any continuous perturbation which induces mode mixing, is able to encode spatially resolved information in its wavelength spectrum.

An attempt was made to generalise to temperature distributions which were not seen during model training with limited success. This has been attributed to the changing polarisation state of light in the fibres and a solution in the form of using polarisation maintaining fibre is suggested.

Although not explicitly shown in this work, this work can be extended to temperature sensing above 1300℃ with the sapphire fibre, temperatures which silica fibre can not be used for. To achieve the calibration at these temperatures, one would use thermocouples. After calibration, the fibre sensor would have all the advantages that fibre sensors possess over the thermocouples, such as small size and electromagnetic passivity.

There are still directions that this line of research could continue from here. The temperature distributions used were all similar in that the temperature monotonically decreased from inside the furnace to out. The DNN would need to be trained on a wider variety of temperature distributions to improve the generalisation capabilities needed for deployment in the field. Another logical direction to take is to attempt to give a regular, translationally invariant fibre distributed sensing capabilities by inducing mode mixing along its length through mechanisms such as perturbing its radius or refractive index. Methods to achieve suitable perturbations could include stress and pressure induced perturbations, tapering or a low power splicing arc. Sapphire fibre has inherent drawbacks such as high cost,

high loss and overall being difficult to work with, and so finding a way to achieve the same effect with regular, silica fibre could make investigating this phenomenon much more accessible.

4 Conclusion

In this thesis, deep learning for regression based fibre optical sensing has been investigated in two ways that have not previously been attempted. Deep learning has been applied to fibre specklegram sensing for temperature and refractive index sensing, displaying improvements over the current statistical methods of specklegram analysis. Deep learning was then applied to fibre reflection spectra for distributed temperature sensing with sapphire optical fibre.

In chapter 2, deep learning analysis of specklegrams from an exposed core fibre for temperature and refractive index sensing was investigated. The advantages of the deep learning method over a conventional statistical correlation method (as used in [29]) is demonstrated. Although it is peripheral to the aims of this thesis, it is worth noting that this previous work demonstrated the first instance of fibre specklegram sensing with an exposed core fibre, hence the first instance of fibre specklegram refractive index sensing. Two different deep neural network architectures, a multi-layer perceptron model and a convolutional neural network, were used. Both of these models were trained on specklegrams from the fibre under i) various temperatures and ii) various depths of water immersion, and compared to the zero-normalised cross correlation function method of analysis, which is standard in current literature. It is shown that the neural networks outperform the correlation method for sensing, improving on such flaws as limited dynamic range and vulnerability to optical misalignment during specklegram recording.

Although deep learning is shown to improve upon the ZNCC method, it is obvious that the full capabilities of the deep learning approach aren't demonstrated. Both the full dynamic range and potential robustness against noise are yet to be seen. The next steps in demonstrating the power of deep learning for fibre specklegram sensing would take this into consideration, i.e. data would be collected over a larger temperature range and a longer

submersion length. Our previous work [62], as well as the work presented in Chapter 3 of this thesis demonstrates that deep learning for temperature sensing works well up to temperatures of 600℃ , and so it would be interesting to investigate whether deep learning models trained on specklegrams are able to function over such a large dynamic range also. Furthermore, as in [62], a logical next step would be to investigate a deep learning model's ability to extract information pertaining to an environmental parameter such as temperature while subjected to strong noise, such as vibration.

This thesis also saw deep learning applied to the wavelength reflection spectra output of multimode fibre for distributed temperature sensing. This is performed with the spectra of unaltered fibres instead of the current method of interferometric fibre temperature sensing which utilises fibre Bragg gratings and wavelength division multiplexing. The idea of spatially unique mode mixing along a fibre leading to spatially unique information in its output is explored, leading to a novel application of sapphire optical fibre's poor diameter consistency for distributed temperature sensing. Experimental data is used to confirm this concept in an experiment which aimed to train deep neural networks with fibre reflection spectra to predict spatially resolved temperature labels. It is shown that the model trained on sapphire fibre spectra far outperforms those trained on spectra from silica fibres which do not share the sapphire fibre's diameter inconsistency, giving more evidence towards continuous mode mixing in a fibre giving it inherent distributed sensing capabilities.

Despite conclusive results, some aspects of this experiment could be improved upon. For instance, all deep learning models, including that trained on sapphire spectra, performed poorly when predicting temperatures from distributions not seen during training. While extrapolating to data outside of the distribution of training data is not something in deep learning which is expected to work often, it is the author's belief that it may be possible. Truly distributed temperature information in the fibre's output should allow for the extraction of temperature information for each individual sensing point

regardless of the overall distribution. It is believed that better extrapolation results could be achieved through the use of a polarisation maintaining fibre setup, so as to minimise noise from changing polarisation states due to moving the sensor. This experiment could have also featured more advanced simulated results, such as simulating transmission through a fibre of more than two sections. Both of these shortcomings were unfortunately a result of the time limit imposed for the completion of the thesis, and the author will be investigating these next steps following the completion of this thesis.

Overall, these two experiments demonstrate the ability of deep learning for regression-based fibre sensing, something which has only been performed once before in the literature [62]. This area of research has much potential for success, if one considers the success of deep learning in almost any other field of research/application. Presented in this thesis is work which demonstrates deep learning's ability to overcome limitations in established fibre sensing techniques, and important steps towards future work which could make deep learning for fibre sensing, along with its many potential advantages over current sensing techniques, practical enough for real world applications.

References

[1] C.K. Kao and G. Hockham. Dielectric fiber surface waveguides for optical frequencies. *Proc. IEE*, 113:1151–1158, 1966.

[2] C. Menadier, C. Kissinger, and H. Adkins. The fotonic sensor. *Instruments and Control Systems*, 40, 1967.

[3] B. Lee. Review of the present status of optical fiber sensors. *Optic. Fiber Technol.*, 9(2):57–79, 2003.

[4] T.W. Krohn, D.A. MacDougall and A. Mendez. *Fiber Optic Sensors: Fundamentals and Applications*. SPIE, fourth edition edition, 2015.

[5] B. Culshaw. Optical fiber sensor technologies: opportunities and-perhaps-pitfalls. *J. Lightwave Technol.*, 22:39–50, 2004.

[6] A. W. Snyder and J. D. Love. *Optical Waveguide Theory*. Chapman and Hall, 1983.

[7] G.B. Hocker. Fiber-optic sensing of pressure and temperature. *Appl. Opt.*, 18(9):1445–1448, 1979.

[8] A. Vali and R.W. Shorthill. Fiber ring interferometer. *Appl. Opt.*, 15(5):1445–1448, 1979.

[9] T. Yoshino, K. Kurosawa, K. Itoh, and T. Ose. Fiber-optic fabry-perot interferometer and its sensor applications. *IEEE Trans. on Mic. Th. Tech.*, MTT-30(10), 1982.

[10] A. Othonos. Fiber bragg gratings. *Rev. Sci. Instrum.*, 68:4309–4341, 1997.

[11] Yu Y., Lui L., H. Tam, and W. Chung. Fiber-laser-based wavelength-division multiplexed fiber bragg grating sensor system. *IEEE Photon. Technol. Lett*, 13(7):702–704, 2001.

[12] R.S. Weis, A.D. Kersey, and T.A. Berkoff. A four-element fiber grating sensor array with phase-sensitive detection. *IEEE Photonics Technology*

Letters, 6(12):1469–1472, 1994.

[13] C. X. Zhou, Yun-Jiang Rao, and Jian Jiang. A coarse wavelength-division-multiplexed extrinsic fiber Fabry-Perot sensor system. In Yun-Jiang Rao, Osuk Y. Kwon, and Gang-Ding Peng, editors, *Advanced Sensor Systems and Applications II*, volume 5634, pages 219 – 224. International Society for Optics and Photonics, SPIE, 2005.

[14] A. Wada, S. Tanaka, and N. Takahashi. Multi-point strain measurement using fabry–perot interferometer consisting of low-reflective fiber bragg grating. *Japanese Journal of Applied Physics*, 56(11):112502, oct 2017.

[15] D. A. Krohn. *Fiber optic sensors*. Instrument Society of America, 2000.

[16] G. Bolognini and A.H. Hartog. Raman-based fibre sensors: Trends and applications. *Opt. Fiber Technol.*, 19(6):678–688, 2013.

[17] T. Horiguchi, K. Shimizu, T. Kurashima, M. Tateda, and Y. Koyamada. Development of a distributed sensing technique using brillouin scattering. *Journal of Lightwave Technology*, 13(7):1296–1302, 1995.

[18] X. Bao. Recent advancements in rayleigh scattering-based distributed fiber sensors. *Adv. Dev. Inst.*, 2021, 2021.

[19] Yunjiang Rao, Zinan Wang, Huijuan Wu, Zengling Ran, and Bing Han. Recent advances in phase-sensitive optical time domain reflectometry (-otdr). *Photonic Sensors*, 11(1):1–30, 2021.

[20] T. Horiguchi, T. Kurashima, and M. Tateda. A technique to measure distributed strain in optical fibres. *IEEE Photon. Technol. Lett*, 2, 1990.

[21] O. Shlomovits, T. Langer, and M. Tur. The effect of source phase noise on stimulated brillouin amplification. *Light Tech. Journal*, 33, 2015.

[22] A. Zadok, E. Zilka, A. Eval, and L. Thévenaz. Vector analysis of stimulated brillouin scattering amplification in standard single-mode fibres. *Opt. Express*, 16, 2008.

[23] A.H. Hartog. A distributed temperature sensor based on liquid-core

optical fibres. *Journal of Lightwave Technology*, 1, 1983.

[24] S. Wu, S. Yin, and F.T.S. Yu. Sensing with fiber specklegrams. *Appl. Opt.*, 30(31):4468–4470, 1991.

[25] A. Leal-Junior, A.G. Frizera, C. Marques, and M.J. Pontes. Optical fiber specklegram sensors for mechanical measurements: A review. *IEEE Sens. J.*, 20(2):569–576, 2020.

[26] H.S. Efendioglu. A review of fiber-optic modal modulated sensors: Specklegram and modal power distribution sensing. *IEEE Sens. J.*, 17(7):2055–2064, 2017.

[27] M. Englund, A. Ipatti, and P. Karioja. Fiber optic security monitoring sensor. *Proc. SPIE*, 3099, 1997.

[28] P. Klokoc, I. Lujo, M. Bosiljevac, and N. Burum. Optical sensor system for vibration measuring. *Proc. IEEE 50th Int. Symp. ELMAR*, pages 625–628, 2008.

[29] T. D. Cabral, E. Fujiwara, S. C. Warren-Smith, H. Ebendorff-Heidepriem, and C. M. B. Cordeiro. Multimode exposed core fiber specklegram sensor. *Opt. Lett.*, 45:3212–3215, 2020.

[30] B. Gupta, H.N. Bhargaw, and H.K. Sardana. Qualifying fibre optic temperature sensor using speckle metrology. *Int. Inf. Technol. Knowl. Manage.*, 1(2):337–350, 2008.

[31] S.C. Schneider, Y. Gautam, and B.G. Zagar. Application of a locally operating laser-speckle strain sensor. *IEEE Trans. Instrum. Meas.*, 52(4):1025–1029, 2003.

[32] Byungchoon Yang, Il-Min Lee, and Byoungho Lee. Wavelength detection using optical fiber speckle patterns. In *LEOS 2000. 2000 IEEE Annual Meeting Conference Proceedings. 13th Annual Meeting. IEEE Lasers and Electro-Optics Society 2000 Annual Meeting (Cat. No.00CH37080)*, volume 2, pages 470–471 vol.2, 2000.

[33] Lisa M. Richards, S. M. Shams Kazmi, Janel L. Davis, Katherine E. Olin, and Andrew K. Dunn. Low-cost laser speckle contrast imaging of blood flow using a webcam. *Biomed. Opt. Express*, 4(10):2269–2283, Oct 2013.

[34] W. Spillman, B. Kline, L. Maurice, and P. Fuhr. Statistical-mode sensor for fiber optic vibration sensing uses. *Appl. Opt.*, 28(15):3166–3176, 1989.

[35] A. Dhall, J.K. Chhabra, and N.S. Aulakh. Intrusion detection system based on speckle pattern analysis. *Experimental Techn.*, 29(1):25–31, 2005.

[36] D.M. Dutton and G.V. Conroy. A review of machine learning. *The Knowledge Engineering Review*, 12(4):341–367, 1997.

[37] Y. LeCun, Y. Bengio, and G. Hinton. Deep learning. *Nature*, 521:436–444, 2015.

[38] S.I. Amari. Backpropagation and stochastic gradient descent method. *Neurocomputing*, 5(4):185–196, 1993.

[39] A. Krizhevsky, I. Sutskever, and G. Hinton. Imagenet classification with deep convolutional neural networks. *Proc. Advances in Neural Information Processing Systems*, 25:1090–1098, 2012.

[40] T. Young, D. Hazarika, S. Poria, and E. Cambria. Recent trends in deep learning based natural language processing [review article]. *IEEE Computational Intelligence Magazine*, 13(3):55–75, 2018.

[41] L. Deng, G. Hinton, and B. Kingsbury. New types of deep neural network learning for speech recognition and related applications: an overview. In *2013 IEEE International Conference on Acoustics, Speech and Signal Processing*, pages 8599–8603, 2013.

[42] A.R. Fayjie, S. Hossain, D. Oualid, and D.J. Lee. Driverless car: Autonomous driving using deep reinforcement learning in urban environment. In *2018 15th International Conference on Ubiquitous*

Robots (UR), pages 896–901, 2018.

[43] F. Murtagh. Multilayer perceptrons for classification and regression. *Neurocomputing*, 2(5):183–197, 1991.

[44] S. Albawi, T.A. Mohammed, and S. Al-Azawi. Understanding of a convolutional neural network. *2017 International Conference on Engineering and Technology (ICET)*, 2017.

[45] D. Gloge. Weakly guiding fibers. *Appl. Opt.*, 10(10):2252–2258, Oct 1971.

[46] Ioannis N. Papadopoulos, Salma Farahi, Christophe Moser, and Demetri Psaltis. Focusing and scanning light through a multimode optical fiber using digital phase conjugation. *Opt. Express*, 20(10):10583–10590, May 2012.

[47] Silvio Bianchi and Roberto Di Leonardo. A multi-mode fiber probe for holographic micromanipulation and microscopy. *Lab Chip*, 12:635–639, 2012.

[48] R. S. Becker. *Theory and Interpretation of Fluorescence and Phosphorescence*. Wiley Interscience, 1969.

[49] M. Plöschner, T. Tyc, and T. Čižmár. Seeing through chaos in multimode fibres. *Nat. Photonics*, 9:529–535, 2015.

[50] S. Aisawa, K. Noguchi, and T. Matsumoto. Remote image classification through multimode optical fiber using a neural network. *Opt. Lett.*, 16:645–647, 1991.

[51] N. Borhani, E. Kakkava, C. Moser, and D. Psaltis. Learning to see through multimode fibers. *Optica*, 2018:960–966, 2018.

[52] B. Rahmani, D. Loterie, G. Konstantinou, D. Psaltis, and C. Moser. Multimode optical fiber transmission with a deep learning network. *Light-Sci. Appl.*, 7:69, 2018.

[53] E. Kakkava, N. Borhani, B. Rahmani, U. Teğin, C. Moser, and

D. Psaltis. Deep learning-based image classification through a multimode fiber in the presence of wavelength drift. *Applied Sciences*, 10(11):3816, 2020.

[54] P. Caramazza, O. Moran, R. Murray-Smith, and D. Faccio. Transmission of natural scene images through a multimode fibre. *Nature Communications*, 10, 2019.

[55] Tianliang Wang, Yi Li, Jinchao Tao, Xu Wang, Yanqing Qiu, Bangning Mao, Miaogen Chen, Yanlong Meng, Chunliu Zhao, Juan Kang, Yong Guo, and Changyu Shen. Deep-learning-assisted fiber bragg grating interrogation by random speckles. *Opt. Lett.*, 46(22):5711–5714, Nov 2021.

[56] Roopam K. Gupta, Graham D. Bruce, Simon J. Powis, and Kishan Dholakia. Deep learning enabled laser speckle wavemeter with a high dynamic range. *Laser & Photonics Reviews*, 14(9):2000120.

[57] Y. Shi, Y. Wang, L. Zhao, and Z. Fan. An event recognition method for -otdr sensing system based on deep learning. *Sensors*, 19(15), 2019.

[58] Y. Bai, J. Xing, F. Xie, S. Liu, and J. Li. Detection and identification of external intrusion signals from 33km optical fiber sensing system based on deep learning. *Optical Fiber Technology*, 53:102060, 2019.

[59] Q. Song, C. Zhang, G. Tang, and F. Ansari. Deep learning method for detection of structural microcracks by brillouin scattering based distributed optical fiber sensors. *Smart Materials and Structures*, 29(7):075008, may 2020.

[60] A.R. Cuevas, M. Fontana, L. Rodriguez-Cobo, M. Lomer, and J.M. Lopez-Higuera. Machine learning for turning optical fiber specklegram sensor into a spatially-resolved sensing system. proof of concept. *Journal of Lightwave Technology*, 36(17):3773–3738, 2018.

[61] D.L. Smith, L. V. Nguyen, D.J. Ottaway, T. D. Cabral, E. Fujiwara, C. M. B. Cordeiro, and S. Warren-Smith. Machine learning for sensing

with a multimode exposed core fiber specklegram sensor. *Opt. Express*, 2022.

[62] L. V. Nguyen, C. C. Nguyen, G. Carneiro, H. Ebendorff-Heidepriem, and S. C. Warren-Smith. Sensing in the presence of strong noise by deep learning of dynamic multimode fiber interference. *Photonics Res.*, 9:B109–B118, 2021.

[63] K. Ribeiro, R. Braga Jr., G. Horgan, D. Ferreira, and T. Sáfadi. Principal component analysis in the spectral analysis of the dynamic laser speckle patterns. *Journal of the European Optical Society - Rapid publications*, 9(0), 2014.

[64] Hongli Lv, Shujun Fu, Caiming Zhang, and Lin Zhai. Speckle noise reduction of multi-frame optical coherence tomography data using multilinear principal component analysis. *Opt. Express*, 26(9):11804–11818, Apr 2018.

[65] H Jabbar and Rafiqul Zaman Khan. Methods to avoid over-fitting and under-fitting in supervised machine learning (comparative study). *Computer Science, Communication and Instrumentation Devices*, 70, 2015.

[66] Optica copyright transfer and licensing information. `https://opg.optica.org/submit/review/copyright_permissions.cfm#oal`.

[67] S. C. Warren-Smith, L. V. Nguyen, C. Lang, H. Ebendorff-Heidepriem, and T. M. Monro. Temperature sensing up to 1300oc using suspended-core microstructured optical fibers. *Opt. Express*, 24:3714–3719, 2016.

[68] T. Habisreuther, T. Elsmann, Z. Pan, A. Graf, R. Willsch, and M. A. Schmidt. Sapphire fiber bragg gratings for high temperature and dynamic temperature diagnostics. *Appl. Therm. Eng.*, 91:860–865, 2015.

[69] P. Lu, L. Men, and Q. Chen. Resolving cross sensitivity of fiber bragg gratings with different polymeric coatings. *Applied Physics Letters*, 92(17):171112, 2008.

[70] J. Ma, W. Tang, and W. Zhou. Optical-fiber sensor for simultaneous measurement of pressure and temperature: analysis of cross sensitivity. *Appl. Opt.*, 35(25):5206–5210, 1996.

[71] S.C. Warren-Smith. *Fluorescence-Based Chemical Sensing Using Suspended-Core Microstructured Optical Fibres*. Phd thesis, 2010.

[72] MATLAB, version 9.11.0.1809720, The MathWorks Inc., 2021.

[73] H. Gao, Y. Jiang, Y. Cui, L. Zhang, J. Jia, and L. Jiang. Investigation on the thermo-optic coefficient of silica fiber within a wide temperature range. *Journal of Lightwave Technology*, 36(24):5881–5886, 2018.

[74] R. Kostecki, H. Ebendorff-Heidepriem, S. C. Warren-Smith, and T. M. Monro. Predicting the drawing conditions for microstructured optical fiber fabrication. *Opt. Mater. Express*, 4(1):29–40, 2014.

[75] E. P. Schartner, L. V. Nguyen, D. Otten, Z. Yu, D. G. Lancaster, H. Ebendorff-Heidepriem, and S. C. Warren-Smith. Multi-point high temperature optical fiber sensor. *Proc. of SPIE*, 11200:1120038, 30 December 2019.

[76] Diederik Kingma and Jimmy Ba. Adam: A method for stochastic optimization. *International Conference on Learning Representations*, 12 2014.

Appendix 1: Code used in chapter 2

Presented in this appendix is the code used to process the data and perform the machine learning undertaken in chapter 2. The code was written in Python in the Jupyter online coding platform. The Keras deep learning library, by Google, was used to create and train the deep neural networks. The general aim of the code is as follows; to read in specklegram images which are stored as .png files, process these into arrays that are suitable of being used by DNNs, build a DNN using the Keras library and train this network using the aforementioned arrays.

The first block of code imports all the packages used throughout the program. The function of prominently used packages will be explained as necessary, and documentation on each can be readily found online.

```
# Code block 1: import necessary packages
import numpy as np
import os
import cv2
import pandas as pd
from PIL import Image
from pathlib import Path
import fnmatch
import random as rn
import matplotlib.pyplot as plt
import time
np.random.seed(69)
rn.seed(69)

import keras
from sklearn.model_selection import train_test_split
from keras.models import Sequential
```

```
from keras.layers.core import Dense, Dropout, Activation,
    ↪ Flatten
from keras.layers.convolutional import Convolution2D as Conv2D
from tensorflow.keras.optimizers import Adam, Adadelta, Adamax
from keras.models import Sequential, load_model
from keras.layers import Dense, Conv1D, MaxPooling1D, Flatten,
    ↪ Dropout, Activation, MaxPool2D
from keras.regularizers import l1, l2
from keras.callbacks import EarlyStopping, ModelCheckpoint
from keras.layers import BatchNormalization
from livelossplot.inputs.keras import PlotLossesCallback

from keras import layers
from keras.layers import Input, Add, Dense, Activation,
    ↪ ZeroPadding2D, BatchNormalization, Flatten, Conv2D,
    ↪ AveragePooling2D, MaxPooling2D, GlobalMaxPooling2D
from keras.models import Model, load_model
from keras.preprocessing import image
from keras.utils import layer_utils
from keras.utils.data_utils import get_file
from keras.applications.imagenet_utils import preprocess_input
from IPython.display import SVG
from keras.utils.vis_utils import model_to_dot
from tensorflow.keras.utils import plot_model
from keras.initializers import glorot_uniform
import scipy.misc
from matplotlib.pyplot import imshow
%matplotlib inline

import keras.backend as K
K.set_image_data_format('channels_last')
```

```
K.set_learning_phase(1)
```

Code block 2 defines a function which will read in the specklegram images from .png files to NumPy arrays using the "cv2" image manipulation package. The .png images are stored to a hard drive in a system such that all images pertaining to a temperature/immersion depth label's video are stored inside a folder named after that label, and each image inside a label folder is labelled as "frame" plus the chronological number of that image as a frame in the original video. This makes for the convenient, automatic importing of the entire archive of images using for loops.

```
# Code block 2: Reading and storing images as arrays
# Set image size for resizing images
image_size_x = 240
image_size_y = 180
image_size_x_original = 800
image_size_y_original = 600

#temps = [4,6,7,8,10,11,12,14]
temps =
    ↪ [22.5,23,23.5,24,24.5,25,25.5,26,26.5,27,27.5,28,28.5,29,29.5,30]
    ↪

def load_data():
    x_data = []
    y_data = []
    x_test = []
    y_test = []
```

```
    for i in range(len(temps)):
        temp = str(temps[i])
        img_folder = "D:/AAA/darcy/Documents/Uni/Masters/
            ↪ Project/ECF_OL_PNG/Air␣Temp␣11-09/" + temp
        for j in range(len(fnmatch.filter(os.listdir(img_folder
            ↪ ), '*.png'))):
            frame = str(j)
            img_path = "D:/AAA/darcy/Documents/Uni/Masters/
                ↪ Project/ECF_OL_PNG/Air␣Temp␣11-09/" + temp + "
                ↪ /" + "frame" + frame + ".png"
            img_colour = cv2.resize(cv2.imread(img_path, cv2.
                ↪ IMREAD_COLOR).astype(np.float32),(image_size_x
                ↪ ,image_size_y))
            img = cv2.cvtColor(img_colour, cv2.COLOR_BGR2GRAY)

            # Code for randomly offsetting images
            #randX = int(round(rn.uniform(-20,20)))
            #randY = int(round(rn.uniform(-20,20)))
            #img = img[270+randX:470+randX,242+randY:442+randY]

            x_data.append(img)
            y_data.append(temps[i])

    x_data = np.array(x_data)
    x_data = np.expand_dims(x_data, axis=3)
    x_test = np.array(x_test)
    #x_test = np.expand_dims(x_test, axis=3)
    y_data = np.array(y_data)
    y_test = np.array(y_test)

    return x_data, y_data, x_test, y_test
```

Code block 3 defines a function which will normalise and remove the positive bias of all values across all arrays in the set of data. It will then shuffle the arays and their associated labels, and split this shuffled set into the training, validation and testing sets required for performing machine learning. The shuffling and splitting is done with the `train_test_split` function from the "sklearn" package, which is designed for this purpose. This function calls the `load_data()` from the previous block of code.

```
# Code block 3:
def normalize_and_split_train_data():
    train_data, train_target, test_data, test_target =
        ↪ load_data()

    #combined_data = np.concatenate((train_data,test_data))
    combined_data = train_data

    m = combined_data.mean()
    s = combined_data.std()

    print ('Train mean, sd:', m, s )
    train_data -= m
    train_data /= s

    train_data1 = np.zeros((np.size(train_data,axis=0),60,60,1)
        ↪ )

    for i in range(np.size(train_data,axis=0)):
        randX = int(round(rn.uniform(-10,10)))
        randY = int(round(rn.uniform(-10,10)))
        #randX = 0
```

```
        #randY = 0
        train_data1[i,:,:,:] = train_data[i,73+randY:133+randY
            ↪ ,81+randX:141+randX,:]

    # 1st split - 10% for testing data - not to be seen during
        ↪  finetuning
    x_train3, x_test2, y_train3, y_test = train_test_split(
        ↪ train_data1, train_target, test_size=0.1,
        ↪ random_state=1)

    # 2nd split - 75/25 of what's left
    x_train2, x_valid2, y_train, y_valid = train_test_split(
        ↪ x_train3, y_train3, test_size=0.25, random_state=1)

    print('Train␣shape:', x_train2.shape)
    print('Validation␣shape:', x_valid2.shape)
    print('Test␣shape:', x_test2.shape)
    return x_train2, x_valid2, y_train, y_valid, x_test2,
        ↪ y_test
```

Code block 4 creates a function which, when called, will create and store the DNN architecture defined within. The code to create the two types of DNN architecture used in the analysis in chapter 2, a VGG style CNN and an MLP, are both shown. The Keras library allows for a simple, modular approach to building DNN architectures by purely adding each layer of the model as a single line of code.

```
# Code block 4a: Defining DNN (3-BLOCK VGG16 MODEL)

def create_model():
    model = Sequential()
```

```
model.add(Conv2D(input_shape=(60,60,1),filters=64,
    ↪ kernel_size=(3,3),padding="same", activation="relu"))
model.add(Conv2D(filters=64,kernel_size=(3,3),padding="same
    ↪ ", activation="relu"))
model.add(MaxPool2D(pool_size=(2,2),strides=(2,2)))

model.add(Conv2D(filters=128, kernel_size=(3,3), padding="
    ↪ same", activation="relu"))
model.add(Conv2D(filters=128, kernel_size=(3,3), padding="
    ↪ same", activation="relu"))
model.add(MaxPool2D(pool_size=(2,2),strides=(2,2)))

model.add(Conv2D(filters=256, kernel_size=(3,3), padding="
    ↪ same", activation="relu"))
model.add(Conv2D(filters=256, kernel_size=(3,3), padding="
    ↪ same", activation="relu"))
model.add(Conv2D(filters=256, kernel_size=(3,3), padding="
    ↪ same", activation="relu"))
model.add(MaxPool2D(pool_size=(2,2),strides=(2,2)))

model.add(Flatten())
model.add(Dense(units=2048,activation="relu"))
model.add(Dense(units=1024,activation="relu"))
model.add(Dense(units=256,activation="relu"))
model.add(Dense(units=1))

return model

# Code block 4b: Defining DNN (MLP MODEL)

def create_model():
```

```
    model= Sequential()

    model.add(Flatten(input_shape=(150,150,1)))
    model.add(Dense(5096, activation='relu'))
    model.add(Dense(1024, activation='relu'))
    model.add(Dense(256, activation='relu'))
    model.add(Dense(64, activation='relu'))
    model.add(Dense(16, activation='relu'))
    model.add(Dense(2))

    return model
```

Code block 5 begins by calling the functions defined above in order to import and process the specklegram data and create the DNN. It then defines hyperparameters related to the training of the DNN, such as the optimiser, number of epochs and loss metric used.

The training itself takes place in the `history = ...` line. Once all the relevant hyperparameters are set, Keras only requires this one line of code to perform the entire training process. All of the mathematics of the stochastic gradient descent process are abstracted away. Once the model is trained, the best model is saved and its performance tested using the validation set.

```
# Code block 5: Training the model

x_train1, x_valid1, y_train, y_valid, x_test1, y_test =
    ↪ normalize_and_split_train_data()
x_train = x_train1
x_valid = x_valid1
x_test = x_test1

es = EarlyStopping(monitor = 'loss', mode = 'min', verbose = 1,
    ↪  patience = 5000)
```

```
mc = ModelCheckpoint('best_model.h5', monitor='loss', mode='min
    ↪ ', verbose=1, save_best_only=True)

model = create_model()

numEpochs = 250

tic = time.perf_counter()

# Setting the optimizer
model.compile(optimizer = Adam(lr=0.001),
              loss = 'mse',
              #metrics = ['accuracy'])
              metrics = ['mse','mae'])

# Run without save best model... not yet
history = model.fit(x_train, y_train, validation_data=(x_valid,
    ↪  y_valid), shuffle = True, batch_size = 64, epochs=
    ↪ numEpochs,
                    verbose=0, callbacks=[PlotLossesCallback(),
                        ↪ es, mc])

toc = time.perf_counter()
print(f"Model␣trained␣in␣{toc␣-␣tic:0.4f}␣seconds")

# load the saved model
saved_model = load_model('best_model.h5')

#predict the value for test spectra with respect to temp (
    ↪ x_test)
predictions = saved_model.predict(x_valid)
```

From here, the performance of the trained model on the validation set can be visualised by plotting its predictions against the true labels (not shown).

The code used to perform the deep learning in chapter 3 is similar to the code shown above. Once the data (1000-point spectra as the x-data and 10 temperature labels as the y-data) had been loaded into suitable NumPy arrays, the normalisation, shuffling and splitting of the data, as well as the building and training of the DNN proceeded as above. An MLP similar to code block 4b was used, except with the correct layer sizes for that task.